

Amplitude Variability and Extracellular Low-Pass Filtering of Neuronal Spikes

Klas H. Pettersen* and Gaute T. Einevoll*[†]

*Department of Mathematical Sciences and Technology, and [†]Center for Integrative Genetics, Norwegian University of Life Sciences, Ås, Norway

ABSTRACT The influence of neural morphology and passive electrical parameters on the width and amplitude of extracellular spikes is investigated by combined analytical and numerical investigations of idealized and anatomically reconstructed pyramidal and stellate neuron models. The main results are: 1), All models yield a low-pass filtering effect, that is, a spike-width increase with increasing distance from soma. 2), A neuron's extracellular spike amplitude is seen to be approximately proportional to the sum of the dendritic cross-sectional areas of all dendritic branches connected to the soma. Thus, neurons with many, thick dendrites connected to soma will produce large amplitude spikes, and therefore have the largest radius of visibility. 3), The spike shape and amplitude are found to be dependent on the membrane capacitance and axial resistivity, but not on the membrane resistivity. 4), The spike-amplitude decay with distance r is found to depend on dendritic morphology, and is decaying as $1/r^n$ with $1 \leq n \leq 2$ close to soma and $n \geq 2$ far away.

INTRODUCTION

Extracellular recordings of electrical activity in the brain are common and easier to carry out than intracellular recordings, particularly *in vivo*. Extracellular potentials are, however, much harder to interpret. In general, they are created by myriads of spatially distributed transmembrane currents summing up in complex ways, each contributing in various degrees to the recorded potential depending on their magnitude, sign, and distance from the recording site (1).

Single electrodes or multielectrodes such as tetrodes are commonly used to record extracellular action potentials (spikes). Traditionally, these recording techniques have been used to count spikes from a single or a few cells, and lately sophisticated methods have been developed for distinguishing, e.g., interneurons from pyramidal cells in such data (2,3). For tetrode recordings, Buzsaki (4) stated that it may be possible to detect pyramidal cells within a radius of 140 μm from the electrode (~ 1000 cells), although only spikes within a radius of 50 μm (~ 100 cells) are separable by currently available clustering methods (4).

Several issues arise when recording spikes from such a relatively large volume, e.g., what types of cells are most likely to be seen in the recordings, which cell parameters are important for the cell's extracellular spike amplitude and shape, and which parameters are important for the decay of the spike amplitude with distance from the neuron? These are important questions also for the interpretation of the multiunit activity (MUA), the high-frequency content of the extracellular potential recorded, e.g., with laminar multi-electrodes (5–7).

In an early study, Rall and Shepherd modeled extracellular potentials related to synaptic interaction and action-potential firing in the olfactory bulb, assuming simplified equivalent-cylinder dendritic geometries of the modeled mitral and granule cells (8). In more recent studies, the extracellular signatures of action-potential firing in morphologically reconstructed pyramidal cells were calculated (9–11). Here compartmental modeling was used to calculate the transmembrane currents, and electromagnetic theory was used in the next step to calculate the extracellular potential at given positions. With active conductances present, this approach requires specification of a vast number of a priori uncertain or unknown parameters describing the ion-channel distribution. The large parameter space makes it difficult to obtain qualitative insights into which aspects of the neuronal morphology or electrical properties affect the extracellular spikes. Here we study the extracellular spike for a set of idealized models for the dendritic structure allowing for extraction of, for example, the qualitative dependence of spike amplitude on distance from soma and passive dendritic parameters. We further test how the features observed in the idealized models transfer to morphologically reconstructed neurons.

Bédard et al. (12) recently investigated the origin of the apparent low-pass filtering of extracellular spikes: spikes recorded far away from the soma contain less signal at higher frequencies than spikes recorded close to the soma. They found that a point-source current cannot produce a frequency-dependent attenuation in a homogenous extracellular medium, nor in a medium with a sinusoidally varying extracellular conductivity (mimicking inhomogeneities). However, they found that a medium of radially exponential decaying extracellular conductivity around the source produces the desired frequency-dependent attenuation (12).

Here the spatial extent of the neuronal morphology will be suggested as an alternative explanation for the low-pass

Submitted May 24, 2007, and accepted for publication September 24, 2007.

Address reprint requests to Gaute T. Einevoll, Tel.: 47-64965433; E-mail: gaute.einevoll@umb.no.

Editor: Arthur Sherman.

© 2008 by the Biophysical Society
0006-3495/08/02/784/19 \$2.00

doi: 10.1529/biophysj.107.111179

filtering effect of extracellular spikes. The net current crossing a neuron's membrane is zero by Kirchhoff's current law. The overall monopolar contribution will thus be zero, and the lowest possible nonzero multipole term will thus be the dipole (1). Here it will be shown that a low-pass filtering effect arises simply due to spatial separation of the resulting current sources and sinks in conjunction with a spike, even in a purely resistive and homogenous extracellular medium.

The six neuron models considered are shown in Fig. 1. We use numerical simulations to study the extracellular spikes for the reconstructed pyramidal and stellate cell models, while the four simplified neuron models (the ball-and-stick neuron, ball-and-star neuron, ball-and-bush neuron, and ball-and-cloud neuron) also allow for analytical investigations. The latter three neuron models are introduced here. The main scope is to study how the neuron's morphology and passive electrical parameters lead to a low-pass filtering effect depending on the distance from soma and thus influence the

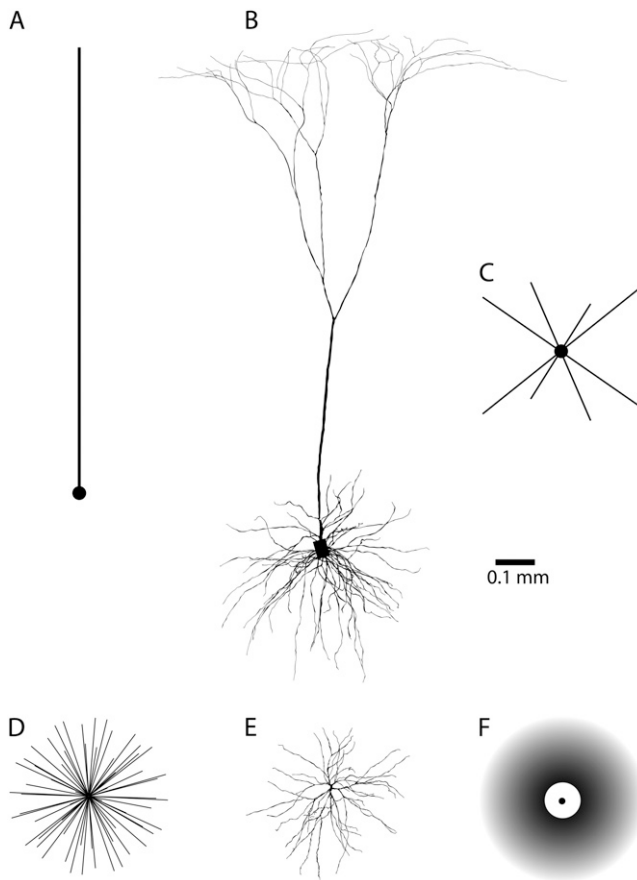


FIGURE 1 The six neuron models used in the study. (A) Ball-and-stick model, (B) reconstructed layer five pyramidal cell, (C) ball-and-star model, consisting of eight dendritic sticks with orientation from a cube's center to its corners, (D) ball-and-bush model, consisting of 60 dendritic sticks evenly spread out in space following a buckyball pattern (16), (E) reconstructed layer four stellate cell, and (F) ball-and-cloud model. The morphology of the reconstructed cells, panels B and E, are the same as in Mainen and Sejnowski (21), downloaded from SenseLab (<http://senselab.med.yale.edu/>).

extracellular spike amplitude and width. We therefore only consider neuron models with passive dendrites and no axons. With active ion channels in the soma only, the modeling procedure can be simplified: Instead of explicitly adding active ion channels to the soma, a prespecified somatic action potential (AP) can simply be imposed as a boundary condition. The transmembrane currents throughout the neuron will in this scheme be identical to the currents found in a model with active somatic ion channels fine-tuned to produce the imposed action potential. This opportunity of imposing the same intracellular AP on all cell models makes it easier to compare how the different cell types translate an AP into an extracellular spike for the different cell types.

All neuron models in Fig. 1 are found to provide the low-pass filtering effect of extracellular spikes. The distance-dependence of the amplitude is found to vary between the models. However, for large distances the amplitude is typically found to decay as $1/r^n$ where n varies between 2 and 3. We also find that the neuronal parameter most strongly determining the amplitude is the diameter of the dendrites connected to soma, and a rough rule of thumb is proposed: a neuron's extracellular spike amplitude is approximately proportional to the sum of the cross-sectional areas of all dendritic branches connected to the soma. The amplitude is further found to depend on the membrane capacitance and axial resistivity, but not on the membrane resistivity.

THEORY

The extracellular potential of a particular action potential (AP) waveform is computed both for idealized neuron models and for morphologically reconstructed cells. The intracellular AP can be expressed as a sum of sinusoids, and since passive cable theory is linear, the extracellular response of each frequency component can be evaluated separately by imposing an alternating-voltage boundary condition in the soma. The extracellular response to a spike is then given by an appropriately weighted sum over the contributions from all frequencies. This separation into individual frequency components also allows for analytical investigations of idealized neuron models. Here the theory behind the calculations is presented.

Extracellular potentials

The extracellular medium is assumed to be homogeneous, purely resistive and infinite in extent with conductivity σ . The potential Φ from a point current source I at time t is, in the quasistatic approximation to Maxwell's equations, given by

$$\Phi(r, t) = \frac{1}{4\pi\sigma} \frac{I(t)}{r}, \quad (1)$$

where r is the distance from the point source (1). Due to the linear nature of Maxwell's equations, the extracellular potential sums up linearly when several point sources are present.

Neuron models

Four idealized neuron models were used in the study: a ball-and-stick neuron (Fig. 1 A), an idealized stellate cell with eight sticks (denoted ball-and-star neuron, Fig. 1 C), an idealized stellate cell with 60 sticks (ball-and-bush neuron, Fig. 1 D), and a neuron model consisting of soma surrounded by a spherically symmetric and continuous dendritic cloud (ball-and-cloud neuron, Fig. 1 F). Two reconstructed neurons, a layer 5 pyramidal cell from cat visual cortex (Fig. 1 B) and a layer 4 stellate cell from cat visual cortex (Fig. 1 E), were also studied.

Reconstructed neurons

Compartmental modeling was used to calculate the transmembrane currents associated with an AP for the reconstructed neurons in the simulation tool NEURON (13). The line-source method from Holt and Koch (9) was used to calculate the contribution to the extracellular potential from each dendritic segment. Instead of treating the transmembrane current from each segment as a point current, this method assumes the segments to be line-current sources with constant current densities. The contribution to the extracellular potential from the current $I_k(t)$ in segment k , assumed evenly distributed over the segment length Δs_k , can be found analytically, and the potential of an N-segmental neuron is found to be (14)

$$\Phi(\vec{r}, t) = \sum_{k=1}^N \frac{I_k(t)}{4\pi\sigma\Delta s_k} \log \left| \frac{\sqrt{h_k^2 + \rho_k^2} - h_k}{\sqrt{l_k^2 + \rho_k^2} - l_k} \right|. \quad (2)$$

Here ρ_k is the distance perpendicular to the line segment, h_k is the longitudinal distance from the end of the segment, and $l_k = \Delta s_k + h_k$ is the longitudinal distance from the start of the segment. The contribution from the transmembrane soma current was modeled by using the point-source formula in Eq. 1.

Ball-and-stick model

In the case of a straight dendritic stick of length l and diameter d lying along the positive z axes, Eq. 1 translates to an integral over the linear transmembrane current density $i_m(z)$,

$$\Phi(z, \rho) = \frac{1}{4\pi\sigma} \int_0^l \frac{i_m(z') dz'}{\sqrt{(z-z')^2 + \rho^2}}, \quad (3)$$

where ρ is the radial distance from the recording point to the stick axis. For a passive dendritic stick of constant diameter, an expression for the transmembrane current $i_m(z)$, including both the linear leak current and the capacitive current, can be found from the cable equation. For a sinusoidally varying membrane potential imposed as a boundary condition at the soma end, the transmembrane current can easily be com-

puted. With complex notation (boldface), the membrane potential is expressed as $\mathbf{V}(z, \omega, t) = \hat{\mathbf{V}}(z, \omega) \exp(j\omega t)$, where the complex $\hat{\mathbf{V}}(z, \omega)$ contains both the amplitude and the phase of the potential, and ω is the angular frequency, $\omega = 2\pi f$. The measured AC potential (or current) will then be the real part of the complex potential (current). For a finite stick with the boundary condition $\hat{\mathbf{V}}_0(\omega)e^{j\omega t}$ in $z = 0$ and a sealed end in $z = l$, a general solution to the alternating current cable equation is (see Appendix A)

$$\hat{\mathbf{V}}(z, \omega) = [e^{sz/\lambda}/(1 + e^{2sl/\lambda}) + e^{-sz/\lambda}/(1 + e^{-2sl/\lambda})] \hat{\mathbf{V}}_0(\omega). \quad (4)$$

The frequency dependence comes in via the complex number $\mathbf{s} = \sqrt{1 + j\omega\tau}$, where $\tau = R_m C_m$ is the membrane time constant, and λ is the direct current (DC) length constant given by $\lambda = \sqrt{dR_m/4R_i}$. The quantities R_m , C_m , and R_i are the specific electric parameters: the membrane resistivity, the membrane capacitance, and the dendrite axial resistivity, respectively. The transmembrane current density is proportional to the double spatial derivative of the membrane potential, and can therefore, in the frequency domain, be expressed as $\hat{\mathbf{I}}_m(z, \omega) = \mathbf{H}(z, \omega) \hat{\mathbf{V}}_0(\omega)$, with

$$\mathbf{H}(z, \omega) = \frac{\pi s^2 d}{R_m} [e^{sz/\lambda}/(1 + e^{2sl/\lambda}) + e^{-sz/\lambda}/(1 + e^{-2sl/\lambda})] \quad (5)$$

(see Appendix A). For a ball-and-stick neuron, the transmembrane soma current $\hat{\mathbf{I}}_s(\omega)$ has to equal the negative of the axial current that goes into the dendrite at its soma end, $\hat{\mathbf{I}}_i(z = 0, \omega)$, and can be expressed as $\hat{\mathbf{I}}_s(\omega) = \mathbf{Y}(\omega) \hat{\mathbf{V}}_0(\omega)$, where $\mathbf{Y}(\omega)$ is the admittance given by

$$\mathbf{Y}(\omega) = \frac{\pi d^{3/2} \mathbf{s}}{2\sqrt{R_i R_m}} [1/(1 + e^{2sl/\lambda}) - 1/(1 + e^{-2sl/\lambda})] \quad (6)$$

(see Appendix A). Note that the prefactor $\pi d^{3/2}/(2\sqrt{R_i R_m})$ in Eq. 6 corresponds to the inverse of the resistance R_λ defined in Dayan and Abbott (15). R_λ corresponds to the total membrane resistance in a section of the cable with length λ or alternatively the total axial resistance along the same cable section.

The complex extracellular potential for a given angular frequency ω can therefore be expressed as $\hat{\Phi}(\rho, z, \omega) = \mathbf{T}(\rho, z, \omega) \hat{\mathbf{V}}_0(\omega)$ with the (complex) transfer function \mathbf{T} given by

$$\mathbf{T}(\rho, z, \omega) = \frac{1}{4\pi\sigma} \left[\int_0^l \frac{\mathbf{H}(z', \omega)}{\sqrt{(z-z')^2 + \rho^2}} dz' + \frac{\mathbf{Y}(\omega)}{\sqrt{(z-z_s)^2 + \rho^2}} \right]. \quad (7)$$

To account for a finite-sized soma, a spherical soma with a radius of $|z_s|$ positioned at the z -axis in $z = z_s < 0$ has been

assumed. The soma is thus attached to the lower end of the dendrite at $z = 0$.

Since the DC-subtracted intracellular somatic AP $V(t)$ can be expressed as a Fourier series, $V(t) = \sum_{k=1}^{\infty} \text{Re}\{\hat{V}_0(\omega_k) e^{j\omega_k t}\}$, the measured extracellular response to any DC-subtracted somatic potential can be expressed as

$$\Phi(\rho, z, t) = \sum_{k=1}^{\infty} \text{Re}\{\mathbf{T}(\rho, z, \omega_k) \hat{V}_0(\omega_k) e^{j\omega_k t}\}. \quad (8)$$

Ball-and-star neuron

The ball-and-star neuron consists of a soma placed in the center of a virtual cube, with eight sticks protruding out from the soma to the cube's corners (Fig. 1 C), and the extracellular potential is computed by a superposition of eight ball-and-stick models through Eqs. 7 and 8. In these plots, the extracellular potentials along an axis going through the soma and the center point of one of the cube's side faces are considered.

Ball-and-bush neuron

Similar to the ball-and-star neuron the ball-and-bush neuron consists of a soma with 60 equally long sticks protruding out from the soma. All stick ends have the same distance to their three closest neighbors (Fig. 1 D), and are positioned at the vertices of a so-called buckyball (16). The extracellular potential is computed by a superposition of 60 ball-and-stick models through Eqs. 7 and 8. In the plots, the extracellular potentials along an axis going through the soma and a center point of a pentagon of sticks in the buckyball structure are considered.

Ball-and-cloud neuron

The ball-and-bush neuron has a so-called closed-field dendritic structure. Due to the approximately spherical symmetry, the electrical potential outside the dendritic region will be small. However, when the recording electrode is positioned inside the periphery of the dendrites, a larger potential will be recorded. Such a neuron may be approximated as a somatic point source surrounded by a spherically symmetric, continuous dendritic cloud of current-source density (Fig. 1 F), created by spherically averaging the total transmembrane currents of N dendritic sticks. The perfect spherical symmetry of the transmembrane currents implies that the extracellular potential will be independent of the angular direction and only depend on the radial distance from the soma origin. Further, Gauss' law implies that the potential at a particular distance r from soma will only depend on the current source inside the sphere of radius r .

The extracellular potential can be expressed in terms of Eq. 8 with the transfer function for the ball-and-cloud model given by (see Appendix B)

$$\mathbf{T}(r, \omega) = \frac{Nd^{3/2}\mathbf{s}}{8r\sqrt{R_i R_m}} \left(\frac{e^{s(r-r_s)/\lambda}}{1 + e^{2sl/\lambda}} - \frac{e^{-s(r-r_s)/\lambda}}{1 + e^{-2sl/\lambda}} \right) \quad (9)$$

for $r_s < r < l + r_s$ and zero for $r > l + r_s$. N corresponds to the number of dendrites, l to the dendritic length, and r_s to the somatic radius.

Approximate extracellular response of ball-and-stick neuron

AC space constant for transmembrane currents

At all times during an action potential, the net current entering the neuron through the membrane is zero. For example, during the initial depolarization phase, current enters the soma, and an equally sized current leaves the dendrites. A main factor determining the size and shape of the extracellular signature is the distance between these current sinks and sources. A neuronal length constant qualitatively describing this sink-source separation can be defined for a ball-and-stick neuron. This length constant does not only give qualitative insights into the extracellular AP signature of a ball-and-stick neuron; it also provides insights of the AP signatures of the ball-and-star and ball-and-bush models which can be considered to be a superposition of several ball-and-stick models.

For the DC condition, i.e., when the soma potential has a fixed constant value, the length constant λ for an infinite stick is defined to be the length over which the potential falls to a fraction $1/e$ of its original maximum value. λ also corresponds to the mean of the normalized transmembrane current weighted by the distance. Similar to this, we define an AC length constant $\lambda_{AC}(\omega)$ as the mean of the absolute value of the current amplitude weighted with distance. For a finite stick, this corresponds to

$$\lambda_{AC}(\omega) = \frac{\int_0^l z \sqrt{\mathbf{I}_m^* \mathbf{I}_m} dz}{\int_0^l \sqrt{\mathbf{I}_m^* \mathbf{I}_m} dz} \quad (10)$$

and for an infinite stick, this simplifies to

$$\lambda_{AC}^{\infty}(\omega) = \lambda \sqrt{\frac{2}{1 + \sqrt{(\omega\tau)^2 + 1}}} \quad (11)$$

(see Appendix C). For the infinite stick, this is identical to the AC length constant defined by the decay of the AC membrane potential envelope (17).

Note, however, that λ_{AC} does not directly correspond to the mean of the physical transmembrane current weighted by distance, but rather the distance-weighted mean of the envelope of the underlying sinusoidally varying transmembrane current. This is seen from the expression of the transmembrane current for an infinite stick,

$$i_m = \text{Re}[\mathbf{i}_m] = -\frac{\pi d}{R_m} \sqrt{1 + (\omega\tau)^2} e^{-z/\lambda_{AC}^{\infty}} \sin(\omega t - kz + \phi) \quad (12)$$

with

$$k = \frac{\omega\tau\lambda_{AC}^{\infty}}{2\lambda^2}, \quad \phi = -\arctan[1/(\omega\tau)] \quad (13)$$

(see Appendix C). From Eqs. 12 and 13 one finds that the zeros of the current expression are separated in the z -direction by the half-wave distance

$$z_0 = \frac{\pi}{k} = \frac{2\pi\lambda^2}{\omega\tau\lambda_{AC}^{\infty}} \approx \pi\lambda_{AC}^{\infty}. \quad (14)$$

The last approximation of Eq. 14 is valid for high frequencies ($\omega\tau \gg 1$) where $\lambda_{AC}^{\infty} \approx \lambda\sqrt{2/(\omega\tau)}$. Within a distance z_0 , the current-amplitude envelope is thus decreased by approximately a factor $\exp(\pi) \sim 23$, e.g., most of the signal strength is within one half-wave. The high-frequency approximation of Eq. 14 corresponds to the lower bound of z_0 . For lower frequencies, the half-wave distance z_0 will be larger.

A definition of λ_{AC} based on the instantaneous true membrane current, i.e., interchanging $\sqrt{i_m i_m^*}$ with i_m in Eq. 10, would lead to a time-varying AC length constant $\bar{\lambda}_{AC}(t, \omega)$, (see Eq. 49 in Appendix C). It is not straightforward to obtain qualitative insights from such a time-dependent length constant, but the form of Eq. 49 implies that any effective length constant based on this expression will be proportional to $\lambda_{AC}^{\infty}(\omega)$ in the high-frequency limit ($\omega\tau \gg 1$). Thus we will, in the following, use $\lambda_{AC}^{\infty}(\omega)$ (and $\lambda_{AC}(\omega)$ in Eq. 10 for finite sticks) as a measure for the typical sink-source separation.

Extracellular potential near soma

The extracellular potential near the soma is dominated by the somatic contribution, i.e., the second term of Eq. 7. The transfer function then becomes

$$\mathbf{T}_{\text{near}}(r, \omega) = \frac{1}{4\pi\sigma r} \mathbf{Y}(\omega), \quad (15)$$

where r denotes the distance to soma.

Extracellular potential in the far-field limit

In the far-field limit the dendritic contribution to the extracellular potential is essential. To get qualitative insights into the origin of the high-frequency damping, we now assume as an approximation that all the transmembrane dendritic current of the ball-and-stick neuron is leaving the dendrite through the same position z defined by the AC space constant, i.e., $z = \lambda_{AC}$. An approximate dipole moment of the ball-and-stick neuron can then be defined. This current dipole will be directed along the axis of the dendritic stick and will oscillate sinusoidally with a frequency-dependent strength with amplitude given by $p(\omega) = [|z_s| + \lambda_{AC}(\omega)] |\mathbf{I}_s(\omega)| = L(\omega) |\mathbf{I}_s(\omega)|$, where $|z_s|$ corresponds to the somatic radius, $L(\omega) = |z_s| + \lambda_{AC}(\omega)$ the dipole length, and $|\mathbf{I}_s(\omega)|$ the soma transmembrane current. The transfer function in a

vertical position z and lateral distance ρ from the z axis will in this dipole approximation be

$$\mathbf{T}(z, \rho, \omega) = \frac{1}{4\pi\sigma} \left(\frac{1}{\sqrt{(\lambda_{AC}(\omega) - z)^2 + \rho^2}} - \frac{1}{\sqrt{(z - z_s)^2 + \rho^2}} \right) \mathbf{Y}(\omega), \quad (16)$$

where $z = 0$ corresponds to the position of the soma end of the stick. This transfer function is frequency-dependent and will lead to frequency-dependent damping of the extracellular potential with respect to lateral distance ρ from the soma. Close to the somatic source the potential will, according to its monopole term of Eq. 15, decay as $1/r$. However, in the far-field limit, $r \gg \lambda_{AC}(\omega)$, the transfer function in Eq. 16 can be approximated with its dipole expression (see Fig. 2),

$$\mathbf{T}_{\text{far,d}}(r, \theta, \omega) \approx \frac{1}{4\pi\sigma} \frac{L \cos\theta}{r^2} \mathbf{Y}(\omega), \quad (17)$$

which implies a $1/r^2$ decay. Here θ is the angle with the positive z axis (see Fig. 2).

Two identical dendritic sticks protruding in opposite directions (like, e.g., pairs of oppositely oriented sticks in the ball-and-star neuron) will have no dipole moment and will instead form a linear quadrupole. In the far-field limit the transfer function from such a quadrupole will be given by (see Fig. 2)

$$\mathbf{T}_{\text{far,q}}(r, \theta, \omega) \approx \frac{1}{4\pi\sigma} \frac{L^2(3\cos^2\theta - 1)}{r^3} \mathbf{Y}(\omega). \quad (18)$$

It should be noted that the far-field dipole and linear quadrupole expressions are essentially identical in the lateral direction at the level of the soma ($z = z_s$). Since $\cos\theta = -L/2\rho$,

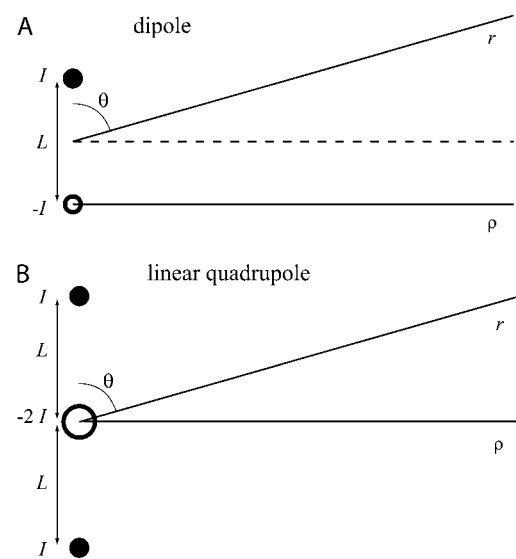


FIGURE 2 Illustration of current dipole (A) and linear current quadrupole (B).

and $r \sim \rho$ in the far-field limit, the dipole expression will decay as L^2/ρ^3 in this direction, half the value of the corresponding extracellular potential from the linear quadrupole. This correspondence is easily understood by the symmetry of the quadrupole: for $\theta = \pi/2$ the lower source can be moved to the position of the upper source without changing its contribution to the resulting potential. Thus the linear quadrupole in Fig. 2 B corresponds to the dipole in Fig. 2 A with twice the dipole strength.

Near the soma, the potential will decay as $1/r$. In the far-field limit the ball-and-stick extracellular potential will, depending on the direction, decay either as $1/r^2$ or $1/r^3$. However, since the AC dipole sizes λ_{AC} are frequency-dependent, the transition to the far-field limit for each frequency component will vary. As we will see in Results, higher frequencies give faster decays of the membrane potential along the dendrites (18) and consequently smaller transmembrane current dipoles. The far-field limit will thus be reached closer to the soma for high frequencies than for low frequencies. As a consequence the higher frequencies will start decaying faster than $1/r$ (i.e., as $1/r^2$ or $1/r^3$) closer to soma than the lower frequencies, and a low-pass filtering effect with respect to distance from soma will occur.

METHODS

Our work focused on two situations:

1. To illustrate the principle behind the frequency damping a 1 Hz and a 100 Hz sinusoidal membrane voltage were imposed as boundary conditions in soma and their relative steady-state extracellular amplitude decays with distance were computed and compared, similar to Bédard et al. (12).
2. A standard action potential (AP) and a narrow AP were enforced as boundary conditions in soma and the extracellular spike-width increases and amplitude decays with distance were computed.

Action potential input

To easily compare spike widths and amplitudes across cell types the same AP was used as boundary condition in the soma for all the cells. The precise shape of the AP was not critical, but we wanted it to be realistic in terms of height, width, and after-hyperpolarization. To produce such an AP we used a Connor-Stevens model (19,20) similar to the one in Dayan and Abbott (15). This was called the standard AP (see Fig. 3). We also used a narrower AP

(labeled *narrow AP* in Fig. 3), simply produced by dividing the unit on the time axis of the standard AP by a factor two. The APs had positive peak amplitudes of 83 mV measured relative to the resting potential, and the spike width measured at half amplitude was 0.55 ms for the standard AP and half this value for the narrow AP. The standard AP was produced in the simulation tool NEURON (13) and saved to file. When the AP later was used as a boundary condition in soma, the baseline was adjusted to zero. The time window used in the simulations was 16.7 ms for the standard AP, and the fundamental frequency was therefore 59.9 Hz.

Reconstructed neurons

The pyramidal and stellate cell models used in these simulations were published in Mainen and Sejnowski (21) and the corresponding NEURON scripts were downloaded from SenseLab (<http://senselab.med.yale.edu/>). NEURON was used to simulate the transmembrane currents during an action potential, with the following model modifications: The axons were removed, all active ion channels were removed from the dendrites and soma, and the soma was treated as an isopotential sphere consisting of one segment only. The reversal potential was set to zero, and the baseline-subtracted AP was used as a boundary condition in soma, executed by NEURON's play command. This could have led to inaccuracies if the inner resistance of the soma had been large enough to produce a drop in potential from the somatic center to the transition points to its dendrites. However, due to the large soma diameter, this potential difference were found to be minimal when experimenting with different somatic intracellular resistivities, but to be on the safe side we used an inner soma resistivity of $R_i = 1 \Omega\text{cm}$ (instead of the value $R_i = 150 \Omega\text{cm}$ used in the dendrites by (21)). Method accuracy was validated by comparing results for the transmembrane currents during an action potential from a NEURON implementation of a finite ball-and-stick neuron with the corresponding results obtained directly by numerical summation of analytical expressions similar to Eqs. 5, 6, and 8.

The transmembrane currents computed in NEURON were written to file with higher accuracy than NEURON's default settings. This was necessary to avoid significant numerical inaccuracies (cancellation errors) when calculating the extracellular potential far from the soma where the small resulting potential essentially is the difference between two relatively large numbers. The extracellular potential was then computed in MatLab (The MathWorks, Natick, MA) using the line-source formula in Eq. 2 based on Holt and Koch (9). To avoid singularities in the extracellular potential, dendritic segments were not allowed to be nearer than $5 \mu\text{m}$ from the recording position. Dendritic segments nearer than $5 \mu\text{m}$ were automatically given a radial distance of $\rho_k = 5 \mu\text{m}$ when using Eq. 2 to compute the extracellular potential.

Geometrical and electrical parameters

Three versions of the ball-and-stick neuron were used, one with infinite length and diameter $d = 2 \mu\text{m}$ (infinite stick), one with length $l = 1 \text{ mm}$ and

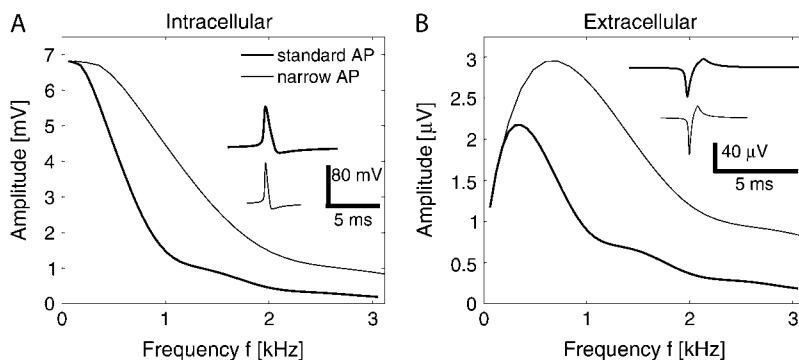


FIGURE 3 (A) Action potentials used in the simulations (*insets*) and their frequency contents. The intracellular spike width is defined as the width of the AP at half amplitude and is 0.55 ms for the standard AP, and half the value for the narrow AP. (B) Frequency contents of the extracellular spikes. (*Inset*) Typical spike shapes for the standard and narrow spike computed a distance $r = 10 \mu\text{m}$ perpendicular to the dendrite at the level of soma for the infinite ball-and-stick neuron. The extracellular spike width is defined as the width of the negative (Na^+) phase at 25% of its maximum amplitude and is 0.44 ms for the spike from the standard AP and 0.22 ms for the spike from the narrow AP. The peak-to-peak value is $56 \mu\text{V}$ for the extracellular spike corresponding to the standard AP and $75 \mu\text{V}$ for the spike corresponding to the narrow AP.

diameter $d = 2 \mu\text{m}$ (long stick), and one with length $l = 0.2 \text{ mm}$ and diameter $d = 1 \mu\text{m}$ (short stick). The finite ball-and-star neuron had soma in the center of a virtual cube, with eight dendritic sticks of length $l = 0.2 \text{ mm}$ and diameter $d = 1 \mu\text{m}$ protruding out toward the cube's corners. The finite ball-and-bush neuron had 60 sticks of the same type evenly spread out in space so that all stick ends had the same distance to its three closest neighbors (16). The finite ball-and-cloud neuron had a spherically symmetric dendritic current density with soma in the center of the cloud. As a basis for obtaining the cloud transmembrane current density, 10 dendritic sticks of the short type ($l = 0.2 \text{ mm}$, $d = 1 \mu\text{m}$) were used. The infinite versions of the above neuron models had sticks with the same diameter but infinite lengths. For all the above neuron models a soma radius of $r_s = 10 \mu\text{m}$ was used. Unless otherwise noted, the membrane and axial resistivities are the same as in Mainen and Sejnowski (21): $R_m = 3.0 \times 10^4 \Omega\text{cm}^2$, $R_i = 150 \Omega\text{cm}$, and the membrane capacitance is $C_m = 1 \mu\text{F}/\text{cm}^2$. The extracellular conductivity was set to 0.3 S/m (22).

For the simplified neuron models (Fig. 1, A, C, D, and F), MatLab was used to evaluate the expressions derived in Theory (see above).

RESULTS

Frequency response of extracellular potential

Fig. 4 A shows the decay of the transmembrane current amplitude with increasing distance from soma for the infinite ball-and-stick neuron. Results are shown for five frequencies for which the AC length constant varies from 1 mm for the 0 Hz to $84 \mu\text{m}$ for the 1500 Hz sinusoids, respectively. In terms of the dipole approximation for the ball-and-stick neuron (Eq. 17), this span in AC length constants implies very different effective dipole sizes. Close to soma the soma current dominates, and the extracellular potential is decaying inversely with the distance from soma (Eq. 1). However, in the far-field limit ($r \gg \lambda_{AC}^\infty$), the potential will decay as a dipole, i.e., inversely with the square of the distance, or the cube of the lateral distance. Since different frequencies correspond to very different dipole sizes, the far-field region is approached nearer the soma for higher frequencies than for lower frequencies. Therefore, a low-pass filtering effect with distance from the neural source will be observed.

Fig. 4 B shows how the dendritic length limits the dipole size. For finite sticks, λ_{AC} in Eq. 10 is always less than half the stick length, and for short dendritic sticks and low frequencies, the dipole length is short. Small, compact neurons therefore tend to show less low-pass filtering with distance from the neuron than larger neurons.

As a measure of the frequency-dependent attenuation of the various components of the extracellular potential, Bédard et al. (12) used the Q_{100} value, $Q_{100} = Z_{100}(r)/Z_1(r)$, where Z_1 and Z_{100} are the effective impedances of the extracellular medium as measured a given distance r from their point source for frequencies of 1 Hz and 100 Hz, respectively. Here we use a similar definition to show the relative frequency damping and define

$$q_{100} = |\hat{\Phi}_{100}(r)|/|\hat{\Phi}_1(r)|, \quad (19)$$

where $|\hat{\Phi}_1(r)|$ and $|\hat{\Phi}_{100}(r)|$ are the amplitudes of the AC extracellular potentials a distance r from the soma for 1 Hz and 100 Hz frequencies, respectively.

Fig. 5 A shows the distance dependence of the q_{100} measure for the infinite and the finite ball-and-stick models ($l = 1 \text{ mm}$), the infinite ball-and-cloud model, the pyramidal neuron, the infinite ball-and-bush model, and the infinite ball-and-star model. For the ball-and-stick neurons and the reconstructed pyramidal neuron we consider positions in the somatic plane perpendicular to the primary apical dendrite of the neuron model. All neurons considered in Fig. 5 A have dendrites of substantial lengths and are seen to have a decay in the q_{100} value with distance, i.e., the 100 Hz amplitude decays faster with distance than the 1 Hz amplitude. The q_{100} value for the pyramidal neuron is based on an average of 36 angular positions in the somatic plane. Results for 12 of these angular positions are shown in Fig. 5 B, illustrating that the q_{100} damping effect is robust in terms of angular position of a recording electrode.

We see in Fig. 5 A that the q_{100} values for the dipole approximation to the infinite-stick model resemble results for the full infinite-stick model. The low-pass filtering of this dipole approximation can be further elucidated by comparing analytical expressions for the q_{100} value near the soma using the expression for \mathbf{T}_{near} in Eq. 15 with the q_{100} value in the far field using the expression for $\mathbf{T}_{\text{far,d}}$ in Eq. 17. In the lateral direction the far-field potential is proportional to L^2/ρ^3 so that with $L \sim \lambda_{AC}^\infty$ we find

$$\frac{q_{100}^{\text{far,d}}}{q_{100}^{\text{near}}} \approx \left(\frac{\lambda_{AC}^\infty(\omega_{100})}{\lambda_{AC}^\infty(\omega_1)} \right)^2 \approx \frac{2}{\omega_{100}\tau} \approx 0.1 \quad (20)$$

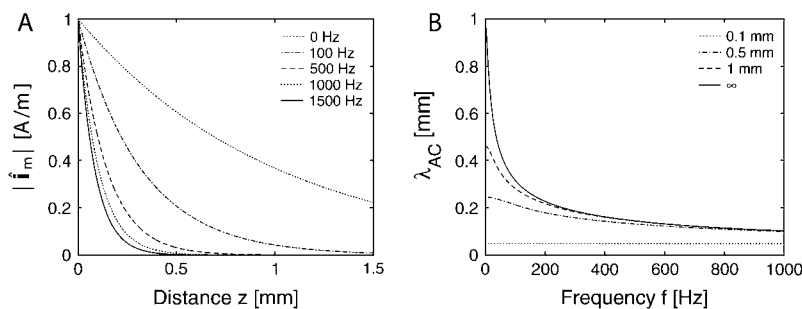


FIGURE 4 (A) Normalized dendritic transmembrane current-density amplitudes for oscillatory somatic potentials as a function of distance from the starting point of the dendrite for an infinite ball-and-stick neuron. Results are shown for five frequencies: 0 Hz, 100 Hz, 500 Hz, 1000 Hz, and 1500 Hz. Stick diameter is $2 \mu\text{m}$. The DC (0 Hz) length constant is 1 mm, and the AC length constants, λ_{AC}^∞ in Eq. 11, is $317 \mu\text{m}$, $145 \mu\text{m}$, $103 \mu\text{m}$, and $84 \mu\text{m}$ for 100 Hz, 500 Hz, 1000 Hz, and 1500 Hz, respectively. (B) The AC length constant, λ_{AC} in Eq. 10, as a function of frequency for sticks of diameter $2 \mu\text{m}$ and length 0.1 mm, 0.5 mm, 1 mm, and infinite length (∞).

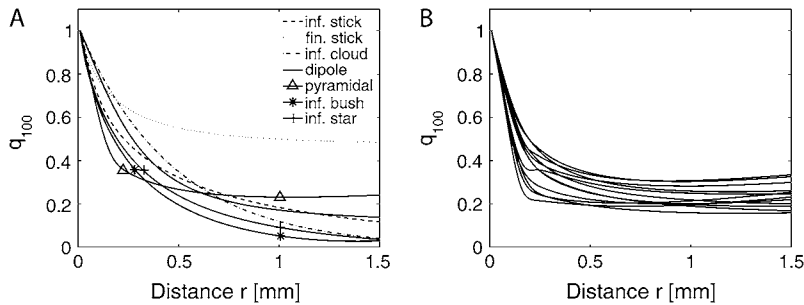


FIGURE 5 (A) q_{100} value, Eq. 19, for the infinite ball-and-stick model (inf. stick), the finite ball-and-stick model (fin. stick) with length $l = 1$ mm, infinite ball-and-cloud model (inf. cloud), infinite ball-and-stick dipole approximation (dipole), pyramidal layer five neuron (pyramidal), infinite ball-and-bush model (inf. bush) and infinite ball-and-star model (inf. star). The ball-and-stick dendrites have diameters of $d = 2 \mu\text{m}$ while the ball-and-bush and ball-and-star stick diameters are $d = 1 \mu\text{m}$. The asymmetric neurons had their stick/primary apical dendrite oriented along the z axis, and the q_{100} values were computed at positions perpendicular to the z axis at the level of the soma. For the pyramidal neuron the q_{100} value was found from averaging q_{100} values for 36 angular positions (every 10th degree) in the lateral (xy) plane. In the dipole approximation the frequency-dependent dipole had length $1006 \mu\text{m}$ for 1 Hz and $327 \mu\text{m}$ for 100 Hz, both values including an assumed somatic radius of $10 \mu\text{m}$. The q_{100} values are all normalized to their values at their starting distance, $r = 10 \mu\text{m}$. (B) q_{100} values for the pyramidal neuron measured at 12 angular positions (every 30th degree) in the lateral plane at the level of the soma.

in good agreement with the dipole results for the largest distances in Fig. 5 A. Here we have used that $\tau = R_m C_m = 30$ ms (see Methods) so that $\omega_{100}\tau = 2\pi \times 100 \times 0.03 \approx 20 \gg 1$ and consequently $\lambda_{AC}^\infty(\omega_{100}) \approx \sqrt{2/\omega_{100}\tau\lambda}$. Further, $\omega_1\tau \approx 0.2$ so that $\lambda_{AC}^\infty(\omega_1) \approx \lambda$.

We further see in Fig. 5 A that the q_{100} value flattens out earlier for the finite-sized neuron models (the finite ball-and-stick model and the pyramidal neuron) where λ_{AC} is significantly reduced by the finite size of the dendrites, especially for the 1 Hz frequency. Flattening occurs when the far-field limit has been reached for both the smaller 100 Hz dipole and the larger 1 Hz dipole.

The finite ball-and-cloud model, finite ball-and-bush model, and the stellate cell were too small to show the high-frequency dampening effect for these low test frequencies. However, when relevant frequencies are higher, like in the action potential, these smaller neuron models will also exhibit a low-pass filtering effect.

Low-pass filtering effects for action potentials

The high-frequency damping effect was not seen in the q_{100} value for, for example, the stellate cell due to the cell's limited size. As seen in Fig. 3 the AP contains a wide range of frequencies, most of them much higher than the frequencies in the q_{100} measure, and the low-pass filtering effect can be expected to manifest itself in the extracellular spike for all neuron models.

A narrow extracellular spike contains higher frequencies than a wide one, see Fig. 3 B. The spike width can therefore be used as a measure of the spike's frequency contents. If the high frequencies are damped more with distance from the neural source than the low frequencies, an increase in spike width should be seen. In Gold et al. (10) the extracellular spike width was defined as the width of the negative phase at 25% of its amplitude, and for a hippocampal pyramidal neuron model with 12 active conductances they report a nearly linear spike-width increase with distance for distances shorter than $100 \mu\text{m}$. Corresponding results for our model neurons are shown in Figs. 6 and 7. As seen in panels 6 A, 6

C, 7 A, and 7 C, the nearly linear increase in spike width with respect to distance from soma reported in Gold et al. (10) is also a feature seen in these purely passive cells for small distances. For the ball-and-stick model with the long dendritic stick of length $l = 1$ mm, the spike width is seen in Fig. 6 to increase almost linearly in most of the distance range. Note that this stick is so long that it has reached the infinite-stick limit; corresponding results for the infinite-stick model overlaid completely these long finite-stick graphs, and it was therefore omitted in the plot. Likewise, the stellate-shaped models with dendrites of infinite extensions (infinite-cloud and infinite-bush) are seen to have a roughly linear increase in spike width in the entire distance range.

However, for the finite-sized cells with shorter dendrites the spike width grows roughly linearly only for soma distances up to $\sim 50 \mu\text{m}$. In Fig. 6, the model with a stick of length $l = 0.2$ mm only (short stick) is seen to exhibit a sublinear increase in spike width for distances larger than $\sim 50 \mu\text{m}$. The same is seen for the finite-size stellate-shaped models in Fig. 7, and here the spike widths are also seen to be almost constant beyond $\sim 100 \mu\text{m}$. This phenomenon can be explained by the finite lengths of the dendrites which limits the effective dipole sizes, especially for the lower frequencies.

Figs. 6 C and 7 C show the spike-width results for the narrow AP. The higher frequencies inherent in this AP reduces the impact of the finite dendritic lengths on the AC dipole size, since the AC dipole sizes are shorter for higher frequencies (see Fig. 4). Thus, the distance from the soma to where the spike-width curves starts to flatten out is larger for the narrow AP than for the standard AP. This is clearly seen by comparing, e.g., results for the short ball-and-stick model in Fig. 6 or the finite ball-and-cloud model in Fig. 7.

As seen for the infinite ball-and-stick neuron with standard AP in Fig. 8, some of the electrical parameters of the neuron also influence the spike width. In Fig. 8, A and B, all parameters have default values except for the diameter, which was set to either one tenth of the default value, the default value or ten times the default value. In Fig. 8, C and D, the inner resistivity was varied, in Fig. 8, E and F, the membrane resistivity was varied; and in Fig. 8, G and H, the

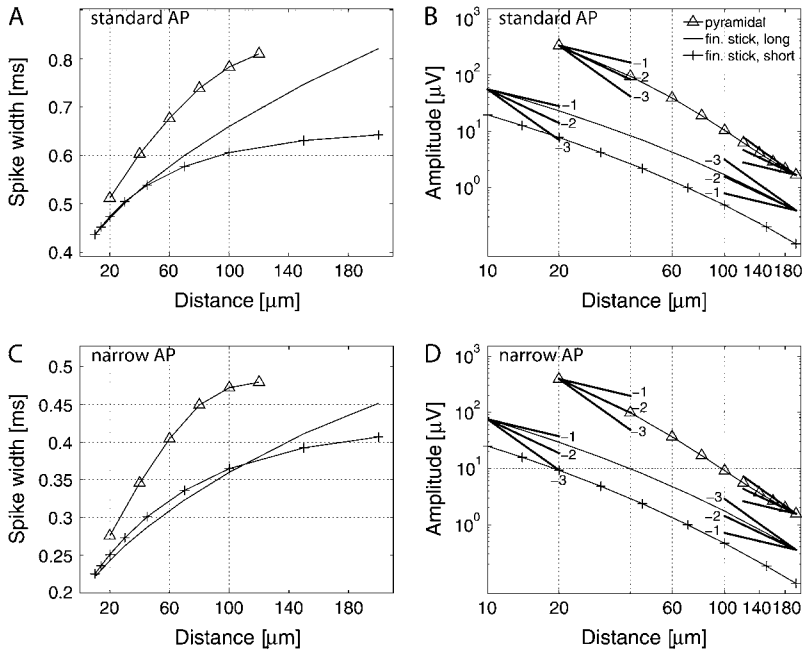


FIGURE 6 Spike widths (A and C) and spike amplitudes (B and D) as a function of distance from soma for the pyramidal cell model (pyramidal) and two types of ball-and-stick models; the long, finite ball-and-stick model (*fin. stick, long*) with diameter $d = 2 \mu\text{m}$ and length $l = 1 \text{mm}$ and the short, finite ball-and-stick model (*fin. stick, short*) with diameter $d = 1 \mu\text{m}$ and length $l = 0.2 \text{mm}$. The somatic input AP in panels A and B is the standard AP of Fig. 3, while the AP in panels C and D is the narrow AP of Fig. 3. The potential is recorded in the somatic plane normal to the stick/primary apical dendrite. For the pyramidal neuron the simulation is based on averaging values for 36 angular directions (every 10th degree). In the spike-width plots results for the pyramidal cell are only shown for distances up to $120 \mu\text{m}$ as the spike shapes were very irregular for larger distances. The infinite ball-and-stick model was omitted in the plot since it was completely covered by the results from the long, finite ball-and-stick model. In panels B and D, guidelines illustrating the power-law decays $1/r$, $1/r^2$, and $1/r^3$ have been added.

membrane capacitance was varied. From Fig. 8 A one sees that a decrease in stick diameter gives a steeper rise of the spike widths, i.e., more increase in high-frequency damping with distance from soma. The same is observed when the inner resistivity R_i (Fig. 8 C) or the membrane capacitance C_m (Fig. 8 F) are increased. However, the membrane resistivity does not influence the high-frequency damping much (Fig. 8 E).

The parameter dependence of the spike-width increases seen in Fig. 8 can be qualitatively understood by considering

the AC length constant for the infinite dendritic stick. For high frequencies ($\omega\tau \gg 1$) the expression of Eq. 11 reduces to

$$\lambda_{AC}^{\infty}(\omega) \propto \frac{\lambda}{\sqrt{\omega\tau}} \propto \sqrt{\frac{d}{f R_i C_m}}, \quad (21)$$

where $\lambda = \sqrt{dR_m/4R_i}$ and $\tau = R_m C_m$ have been used. This approximate expression for λ_{AC}^{∞} implies that a smaller d , a larger R_i , or a larger C_m all reduce the AC space constant, i.e., the effective dipole length. In contrast, the expression for

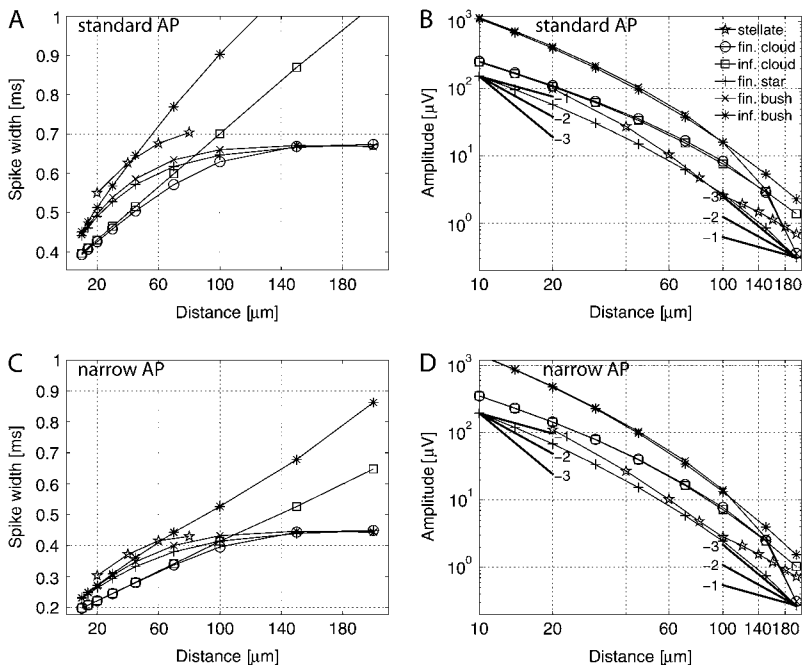


FIGURE 7 Spike widths (A and C) and spike amplitudes (B and D) as a function of distance from soma for the stellate cell (stellate), finite ball-and-cloud (*fin. cloud*), infinite ball-and-cloud (*inf. cloud*), finite ball-and-star (*fin. star*), finite ball-and-bush (*fin. bush*), and infinite ball-and-bush (*inf. bush*) models for the standard (A and B) and narrow AP (C and D). For the stellate cell the simulation is based on averaging results from 60 angular positions spherically distributed around soma (the 60 instances corresponding to the axes of the buckyball (16)). The ball-and-bush neuron model has sixty dendritic sticks of diameter $d = 1 \mu\text{m}$ spread out in its bucky angles, and the potential is measured on an axis going through the soma and the center of one pentagon. The cloud model has transmembrane currents from $N = 10$ sticks homogeneously smoothed out in the angular directions. For large distances from soma, irregular extracellular spikes were seen for the stellate cell, for example, instances with an initial positive (capacitive) peak larger than the later positive repolarization (K^+). These were omitted in the averaging procedure. Even so, in the spike-width plots, results for the stellate cell are only shown for distances up to $80 \mu\text{m}$ as the spike shapes were very irregular for larger distances. In panels B and D, guidelines illustrating the decays $1/r$, $1/r^2$ and $1/r^3$ have been added.

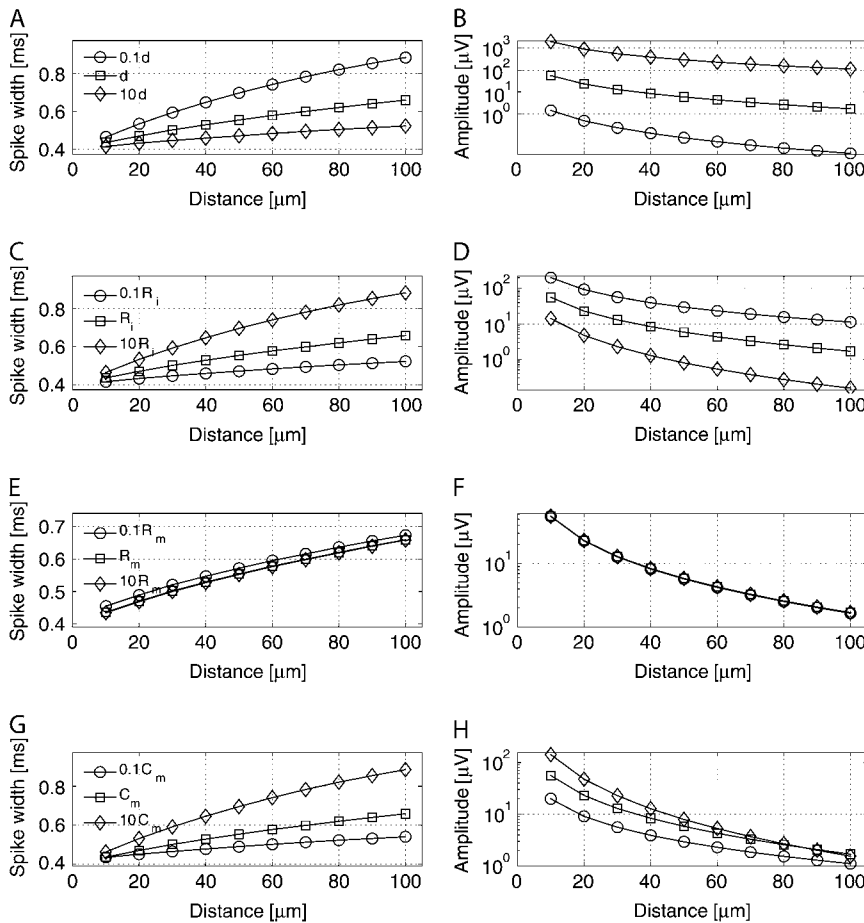


FIGURE 8 Illustration of parameter dependence of spike widths (left column) and amplitudes (right column) for infinite ball-and-stick model and standard AP. The potential is shown as a function of distance from the soma in the somatic plane (at the level of the soma). One parameter was varied in each example: (A and B) variation of diameter, (C and D) axial resistivity, (E and F) membrane resistivity, and (G and H) membrane capacitance. Results are shown with the varied parameter at 1:10th of default value, default value, and 10-times default value, with the other parameters at default values.

λ_{AC}^∞ is found to be effectively independent of the membrane resistivity. A smaller AC length constant for the higher frequencies implies that the transition region, where the salient frequencies switch from their near-soma to their far-field behavior, will occur for smaller distances. As a consequence, more of the increase in spike width will occur closer to soma. For even larger distances (results not shown) the spike width eventually reaches a plateau, approximately at values of 1.5–1.6 ms for the models in Fig. 8. There the far-field limit has been reached for all frequencies inherent in the action potential, and there will be no further high-frequency dampening effect. Here, the choice of membrane parameters imply a time constant of $\tau = 30$ ms, and the approximation $\omega\tau \gg 1$ inherent in Eq. 21 will be valid for frequencies larger than ~ 100 Hz (where $\omega\tau \approx 20$). In the frequency spectrum of the standard AP shown in Fig. 3 B, we see that most of the power lies at frequencies above 100 Hz, so that the approximate expression in Eq. 21 applies for most of the relevant frequencies.

Of the four parameter dependencies plotted in Fig. 8 the diameter and membrane resistivity are the two most likely to vary for real neurons; the dendritic diameters vary from cell to cell, while the membrane resistivity may also vary with the state of the neuron. However, since the variation of the mem-

brane resistivity does not influence the frequency damping much, the diameter of the stick appears to be the important parameter determining the spike-width increase for the infinite ball-and-stick model. For finite ball-and-stick models the stick lengths also influence the damping. Therefore, these results indicate that the geometry of the dendritic tree (number of dendrites, their lengths and widths) is the main factor determining the spike-width increase, and the low-pass filtering effect with distance in general.

Amplitude decay of extracellular spikes

In Fig. 6, B and D, and Fig. 7, B and D, the peak-to-peak spike amplitude as a function of distance from soma is plotted in double-logarithmic plots. Although the models have the same electrical parameters and the same somatic AP, both the overall amplitude differences and the variation in distance dependence is striking.

For the ball-and-stick models, the exponent of the amplitude decay with distance is seen to be between 1 and 1.5 for the shortest distances. The exponent is seen to be slightly smaller for the standard AP than for the narrow AP, i.e., closer to the theoretical soma point-source expression in Eq. 15. This can be understood by the lower frequencies

inherent in the standard AP compared to the narrow AP. This makes the length constant λ_{AC} longer so that the soma point-source contribution dominates in a larger region around the soma. For the largest distances considered in Fig. 6 the spike amplitudes for the ball-and-stick models are seen to decay with an exponent between 2 and 2.5. The observed decay with distance is thus less rapid than the predicted far-field decay $1/r^3$ in this direction (see Eq. 18), reflecting that the largest distance considered in the plot ($r = 200 \mu\text{m}$) is too short for the models to be completely in the far-field limit (see Fig. 10).

For the stellate-shaped idealized models (ball-and-star, ball-and-bush, ball-and-cloud) we see in Fig. 7 that the exponent of the amplitude decay is between 1 and 2 for the shortest distances. At the largest distances the decay has an exponent between 2 and 3 for the infinite ball-and-bush and ball-and-cloud models, while the amplitude drops sharply as the distance approaches $200 \mu\text{m}$ for the finite ball-and-bush and ball-and-cloud models (all with $200\text{-}\mu\text{m}$ -long dendrites). This reflects the approximate (ball-and-bush) and perfect (ball-and-cloud) closed-field dendritic structure of these model neurons. In contrast, the eight symmetrically placed dendrites in the finite ball-and-star neuron is seen to be too sparse to form a similarly effective closed-field structure, and the amplitude is seen to decay slower, roughly as $1/r^3$. For the ball-and-bush models we observe that the finite-dendrite and infinite-dendrite versions of the model have similar amplitudes for distances up to $\sim 120 \mu\text{m}$ where the sharp drop of the finite-model amplitude is initiated. For the ball-and-cloud models the finite and infinite versions are correspondingly seen to have similar amplitude for distances up to $\sim 160 \mu\text{m}$.

For the pyramidal cell in Fig. 6 B, the amplitude decays as $1/r^n$ with an exponent of $n \sim 2$ for the smallest distances considered ($r = 20 \mu\text{m}$), while the exponent increases to $n \sim 2.5$ for distances larger than $r = 60 \mu\text{m}$. The stellate cell of Fig. 7 B has similar decay for small distances, but for distances between $60 \mu\text{m}$ and $100 \mu\text{m}$ the exponent of the decay appears to be $n \sim 3$, while for distances larger than $100 \mu\text{m}$, n appears to be ~ 2 .

Parameter dependence of ball-and-stick extracellular spikes

The parameter dependence of the decay of extracellular peak-to-peak amplitude with distance from soma is shown for the ball-and-stick model in Fig. 8. We see that the dendritic diameter is the parameter having the strongest influence on the extracellular spike amplitude. The intracellular resistivity R_i (Fig. 8 D) and the membrane capacitance C_m (Fig. 8 H) have significant influence as well, while the membrane resistivity plays essentially no role (Fig. 8 F). This can be understood by considering approximate expressions for the extracellular potential close to and far from the soma. Near the soma the somatic current dominates, and the potential is proportional to I_s/r , where I_s is the soma current

(Eqs. 1 and 15). From the transfer function in Eq. 15 and the expression for the somatic admittance for an infinite stick in Eq. 6, one can infer the following parameter dependence of the frequency response for high frequencies ($\omega\tau \gg 1$),

$$|\mathbf{T}_{\text{near}}| = \frac{1}{4\pi\sigma r} \frac{\pi d^{3/2} |\mathbf{s}|}{2\sqrt{R_i R_m}} \propto \frac{d^{3/2} \sqrt{\omega\tau}}{\sigma r \sqrt{R_i R_m}} \propto \frac{d^{3/2}}{\sigma r} \sqrt{\frac{f C_m}{R_i}}, \quad (22)$$

where the relationship $|\mathbf{s}| = ((\omega\tau)^2 + 1)^{1/4}$ has been used. Note that this expression is not only applicable for the ball-and-stick model; it will be similar for all our idealized neuron models.

First, notice that the expression is frequency-dependent. High frequencies will be amplified compared to low frequencies. This implies that the narrow AP of Fig. 3 A will, close to the cell, produce an extracellular spike with higher peak-to-peak amplitude than the standard AP. This is indeed seen to be the case in the example ball-and-stick spikes shown in Fig. 3 B and when the results in Figs. 6 D and 7 D for the short-distance amplitude are compared with Figs. 6 B and 7 B, respectively. Second, although both the inner resistivity and the membrane capacitance are seen to influence the amplitude close to soma ($|\mathbf{T}_{\text{near}}| \propto (C_m/R_i)^{1/2}$), the most important factor is the dendritic diameter ($|\mathbf{T}_{\text{near}}| \propto d^{3/2}$), as seen in Fig. 8.

As the distance from soma increases, one cannot only take the soma current into account; also the effective dipole sizes become important factors determining the extracellular spike amplitude. In the far-field limit of the ball-and-stick neuron one might, if the dipole is not perpendicular to the plotting axis, use the dipole expression of Eq. 17 with $\lambda_{AC}^\infty(\omega)$ from Eq. 21 as an estimate for the dipole length. For high frequencies ($\omega\tau \gg 1$), one finds

$$|\mathbf{T}_{\text{far,d}}| \sim \frac{1}{4\pi\sigma} \frac{\lambda_{AC}^\infty}{r^2} \frac{\pi d^{3/2} |\mathbf{s}|}{2\sqrt{R_i R_m}} \propto \sqrt{\frac{d}{f R_i C_m} \frac{f C_m d^{3/2}}{R_i \sigma r^2}} = \frac{d^2}{\sigma r^2 R_i}. \quad (23)$$

If the dipole is perpendicular to the recording axis, the dipole expression in Eq. 17 becomes essentially identical to the linear quadrupole expression in Eq. 18, i.e.,

$$|\mathbf{T}_{\text{far,q}}| \sim \frac{1}{4\pi\sigma} \frac{(\lambda_{AC}^\infty)^2}{r^3} \frac{\pi d^{3/2} |\mathbf{s}|}{2\sqrt{R_i R_m}} \propto \frac{d^{5/2}}{\sigma r^3 f^{1/2} R_i^{3/2} C_m^{1/2}}. \quad (24)$$

The approximate dipole expression in Eq. 23 is, in addition to the dependence of extracellular conductivity and distance, only dependent on the dendritic diameter and axial resistivity. The quadrupole expression is also dependent on the frequency and the membrane capacitance, although now inversely compared to the monopole expression of Eq. 22. This frequency dependence implies that, opposite to the situation near the soma, the standard AP should have a higher amplitude further away from the source than the narrow AP, because of its higher power on the lower frequencies. This is

indeed seen by close inspection of the large-distance amplitudes of the long finite-stick model in Fig. 6.

The frequency dependence of Eqs. 22–24 also further elucidates the low-pass filtering effect seen extracellularly: close to the soma, the frequency dependence imply that the high frequencies of the somatic potential are enhanced ($|\mathbf{T}| \propto f^{1/2}$); further away, this amplification is lost and the frequency dependence can even become inverted ($|\mathbf{T}| \propto f^{-1/2}$) compared to the monopole expression of Eq. 22.

When moving from the vicinity of the soma to the far-field limit, Eqs. 22 and 24 imply that the exponent in the power-law dependence of the membrane capacitance changes from $1/2$ to $-1/2$. Even if the largest distance considered in Fig. 8 is too short to correspond to the far-field limit, this tendency is clearly seen in Fig. 8H: near the soma the three different choices of C_m give quite different results, while they approach the same value for the largest distances shown; for even larger distances the curves would cross. For the diameter d and inner resistivity R_i , Eqs. 22 and 24 imply that the exponent in the power-law for the diameter should change from $3/2$ to $5/2$ while the exponent for the inner resistivity should change from $-1/2$ to $-3/2$ as one moves from the soma to the far-field limit. This is in qualitative agreement with what is seen in Fig. 8, B and D; the graphs are diverging for larger distances.

The parameter dependence of the extracellular spike amplitude of the infinite ball-and-stick neuron is further illustrated in the two upper rows of Fig. 9. Here the plots show how the amplitude varies with each of the neuronal model parameters d , R_i , C_m , and R_m for three distances: near the soma ($r = 20 \mu\text{m}$), at an intermediate distance ($r = 100 \mu\text{m}$), and at a very large distance corresponding to the far-field limit ($r = 1000 \mu\text{m}$). In the first row the distance dependence when moving laterally out from soma is shown (as in Fig. 8). In the second row the corresponding distance dependence is shown when moving from the soma along a line 30° below the lateral axis, i.e., $\theta = 120^\circ$ (Fig. 2). Near the soma ($r = 20 \mu\text{m}$) the amplitude is in both cases seen to be proportional to $d^{1.5}R_i^{-0.5}C_m^{0.5}$, in agreement with the predictions from Eq. 22. When moving in the lateral direction we see in the first row that for the largest distance ($r = 1000 \mu\text{m}$) the amplitude is proportional to $d^{2.5}R_i^{-1.5}C_m^{-0.5}$, in agreement with the far-field quadrupole expression in Eq. 24. For the intermediate distance ($r = 100 \mu\text{m}$) the parameter dependence is seen to be an intermediate case between the near-soma and far-field expressions: the amplitude is seen to be roughly proportional to $d^2R_i^{-1}$. When moving 30° below the lateral axis (second row), the amplitude for the largest distances ($r = 1000 \mu\text{m}$) is, as expected, seen to be proportional to $d^2R_i^{-1}$, in agreement with the far-field dipole expression in Eq. 23. A similar parameter dependence is seen for the intermediate distance ($r = 100 \mu\text{m}$), i.e., the far-field situation appears to be reached earlier when moving in an angle with the lateral axis than when moving in the lateral direction.

The transition from the monopole to the multipole situations when moving away from the soma is further demonstrated in Fig. 10 where the distance dependence of the extracellular spike amplitudes is shown for the same models considered in Fig. 9. Near the soma the amplitude is seen to decay as $1/r$ (see Eq. 22), while for the largest distances it is seen to decay as $1/r^2$ when moving in a 30° angle below the lateral axis (see Eq. 23) and as $1/r^3$ when moving along the lateral axis (see Eq. 24). We also see that for $r \sim 100 \mu\text{m}$ the amplitude decays roughly as $1/r^2$ in both directions. In Fig. 10 the amplitude decay in the lateral direction is shown both for the infinite ball-and-stick model and the finite ball-and-stick model with stick length $l = 1 \text{ mm}$. As seen in the figure the amplitudes are almost indistinguishable, implying that the infinite-stick limit has essentially been reached for this stick length.

Parameter dependence of ball-and-star extracellular spikes

The ball-and-star model is built up of four linear quadrupoles (see Fig. 2), but the highly symmetric cubic arrangement makes the quadrupole moment zero. The first nonzero multipole moment is the octupole moment, i.e., the multipole of degree four. For this neuron model we thus expect the following far-field behavior,

$$|\mathbf{T}_{\text{far,o}}| \sim \frac{1}{4\pi\sigma} \frac{(\lambda_{\text{AC}}^\infty)^4 \pi d^{3/2} |\mathbf{s}|}{r^5 \sqrt{2R_i R_m}} \propto \frac{d^{7/2}}{\sigma r^5 f^{3/2} R_i^{5/2} C_m^{3/2}} \quad (25)$$

The parameter dependence of the extracellular spike amplitude of the ball-and-star neuron is illustrated in the two bottom rows of Fig. 9. In the third row, results for the ball-and-star model with infinitely long dendrites are shown, while results for the finite-dendrite ($l = 200 \mu\text{m}$) ball-and-star are shown in the fourth row. As for the ball-and-stick models the amplitude near the soma ($r = 20 \mu\text{m}$) is in both cases seen to be proportional to $d^{1.5}R_i^{-0.5}C_m^{0.5}$, in agreement with the predictions from Eq. 22. For the largest distance ($r = 1000 \mu\text{m}$), the amplitude is for the infinite ball-and-star model seen to be proportional to $d^{3.5}R_i^{-2.5}C_m^{-1.5}$, in agreement with the far-field octupole expression in Eq. 25. For the intermediate distance ($r = 100 \mu\text{m}$), the parameter dependence is seen to be an intermediate case between the near-soma and far-field expressions: the amplitude is seen to be roughly proportional to $d^{2.5}R_i^{-1.5}C_m^{-0.5}$.

For the finite ball-and-star model the amplitude is, however, seen to be proportional to $\sim d^{2.5}R_i^{-1.5}C_m^{-0.5}$ for the largest distance ($r = 1000 \mu\text{m}$), i.e., different from the prediction of the far-field octupole expression in Eq. 25. This reflects the short stick length ($l = 200 \mu\text{m}$), which at least for the lower salient action-potential frequencies reduces the effective length constant λ_{AC} of the individual sticks from $\lambda_{\text{AC}}^\infty(f) \sim \sqrt{fd/R_i C_m}$ to lengths of the order $l/2$. The net

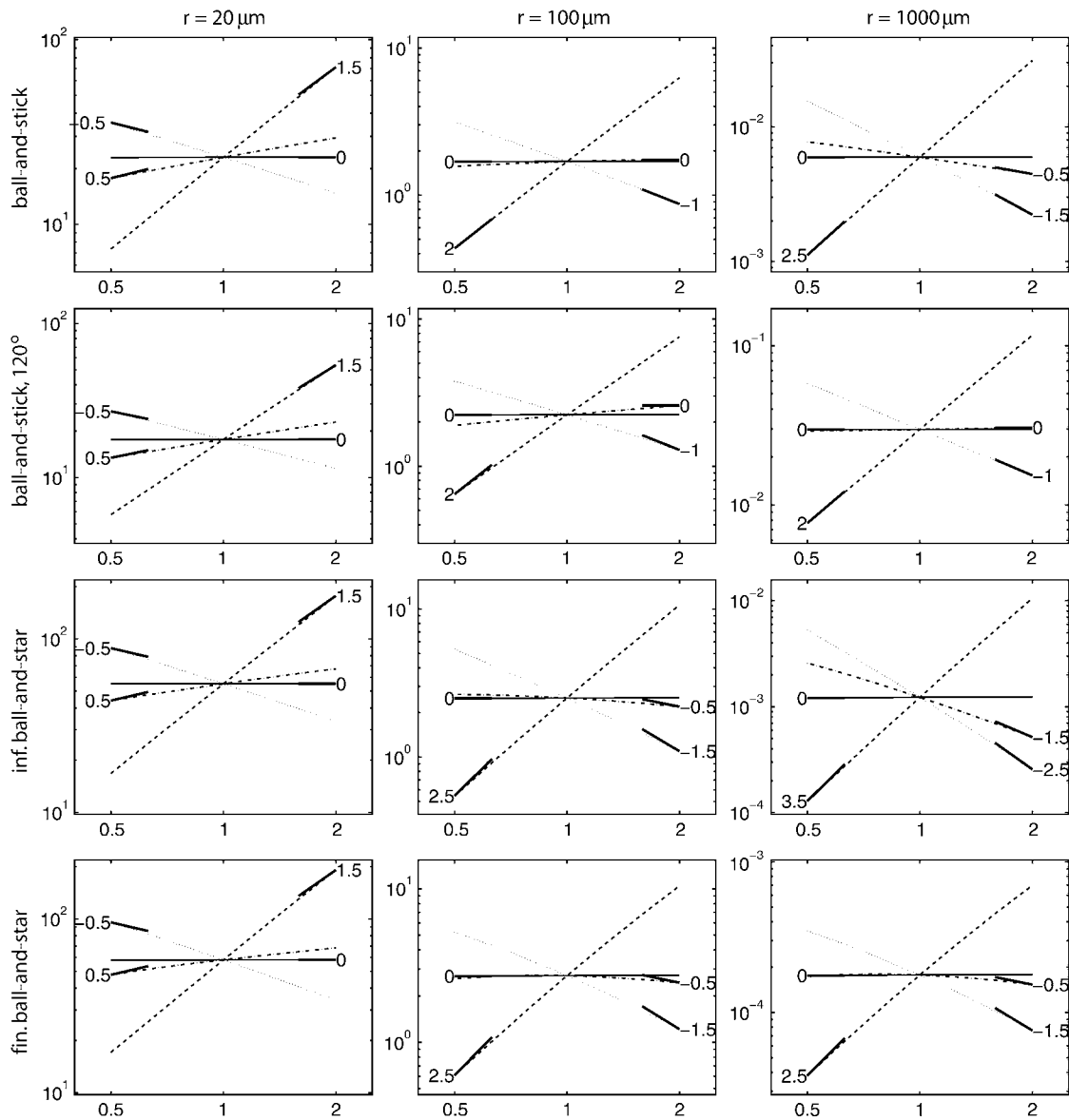


FIGURE 9 Illustration of parameter dependence of extracellular spike amplitude for infinite ball-and-stick model in the lateral direction (*first row*), infinite ball-and-stick model in a direction 30° below the lateral axis, i.e., $\theta = 120^\circ$ (*second row*), infinite ball-and-star model, lateral direction (*third row*), and finite ball-and-star model with dendritic stick lengths of $200 \mu\text{m}$, lateral direction (*bottom row*). In each panel the dependences of the peak-to-peak spike amplitude on the membrane resistivity R_m (*solid line*), the dendritic diameter d (*dashed line*), the axial resistivity R_i (*dotted line*), and the membrane capacitance C_m (*dash-dotted line*) are shown around their default values in a double-logarithmic plot. The x-coordinate corresponds to the parameter value in units of the default parameter value, and results from varying the parameter from half to twice the default values are shown. Only a single parameter is varied at the time; the other three parameter values are kept at their default values. Results are shown for three distances: near the soma ($r = 20 \mu\text{m}$, *left column*), intermediate ($r = 100 \mu\text{m}$, *middle column*), and far away from soma ($r = 1000 \mu\text{m}$, *right column*). Guidelines corresponding to different steepnesses are added. In the short-distance panels ($r = 20 \mu\text{m}$) the guidelines correspond to the theoretical monopole expression in Eq. 22. The guide lines in the large-distance ($r = 1000 \mu\text{m}$) ball-and-stick panel in the first row (*lateral direction*) correspond to the predictions from the far-field quadrupole expression in Eq. 24. The guide lines in the large-distance ($r = 1000 \mu\text{m}$) ball-and-stick panel in the second row ($\theta = 120^\circ$) correspond to the predictions from the far-field dipole expression in Eq. 23. The guide lines in the large-distance ($r = 1000 \mu\text{m}$) infinite ball-and-star panel in the third row correspond to the predictions from the far-field octupole expression in Eq. 25. In the remaining five panels guidelines with similar slopes as the observed curves have been added. The y-axis unit is μV .

result reflects the weighted sum over contributions from low frequencies where $\lambda_{AC} \sim l/2$ and high frequencies where $\lambda_{AC} \sim \lambda_{AC}^\infty \sim \sqrt{fd/R_i C_m}$, and a parameter dependence intermediate between the near-soma situation ($d^{3/2} R_i^{-1/2} C_m^{1/2}$)

and the far-field quadrupolar situation ($d^{7/2} R_i^{-5/2} C_m^{-3/2}$) is observed.

The transition from the monopole to the octupole situation when moving away from the soma is shown in Fig. 10. Both

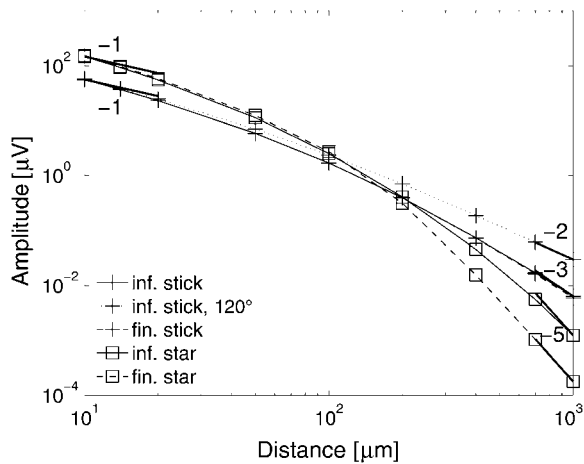


FIGURE 10 Illustration of distance dependence of extracellular spike amplitude for the same models and directions as in Fig. 9. Results for the finite ball-and-stick model amplitude ($l = 1$ mm) as a function of distance in the lateral direction are also shown. All parameters have their default values (see Methods). Results are shown in a double-logarithmic plot, and guidelines corresponding to different steepnesses are added at the shortest and largest distances considered. At the shortest distance ($r = 10 \mu\text{m}$), the guidelines correspond to the theoretical monopole expression $1/r$ from Eq. 22. For the largest distance ($r = 1000 \mu\text{m}$), the guideline $1/r^3$ at the ball-and-stick results for the lateral direction corresponds to the predictions from the far-field quadrupole expression in Eq. 24. For the infinite ball-and-stick results in the direction $\theta = 120^\circ$, the guideline $1/r^2$ corresponds to the predictions from the far-field dipole expression in Eq. 23. For the ball-and-star results, the added guidelines ($1/r^5$) correspond to the prediction from the far-field octupole expression in Eq. 25.

for the infinite and finite ball-and-star models the amplitude is seen to decay as a $1/r$ near the soma (see Eq. 22), while it is seen to decay, for the largest distances, approximately as $1/r^5$ (see Eq. 25). Thus while the dependence of the amplitude on the dendritic parameters d , R_i , and C_m is strongly affected by the short dendritic sticks in the finite ball-and-star model, the distance dependence is not. The potential is still effectively an octupole in the far-field limit, but the effective source length constant λ_{AC} is in the finite ball-and-star model limited by the dendritic length and differs from the infinite-stick length constant $\lambda_{AC}^\infty \sim \sqrt{fd/R_i C_m}$ inherent in Eq. 25. Since the finite-sticks limit the length constants, the far-field limit is expected to be reached earlier for the finite ball-and-star model than for the infinite ball-and-star model. This is indeed seen in Fig. 10 where the amplitude of the finite model is seen to decay as $1/r^5$ for distances approaching $1000 \mu\text{m}$, while the far-field limit has not been completely reached for the infinite model so that the decay has a slightly lower power than five.

For distances between 100 and $200 \mu\text{m}$, the parameter dependence ($\sim d^{2.5} R_i^{-1.5} C_m^{-0.5}$) in Fig. 9 and distance dependence ($\sim 1/r^3$) in Fig. 10 imply a behavior similar to the quadrupolar expression in Eq. 24 for the ball-and-star models. Thus in this distance range one expects $|\mathbf{T}| \propto 1/\sqrt{f}$, i.e., a dampening of higher frequencies, so that the standard

AP should have a higher peak-to-peak amplitude as compared to the narrow AP. This effect is seen by inspection of the amplitudes of the ball-and-star model results in this distance range in Fig. 7. The same effect is also seen for the ball-and-bush and ball-and-cloud models in the same figure.

DISCUSSION

The impact of cell morphology and passive electrical parameters on the extracellular spike amplitude and width, as well as the low-pass filtering effect of individual frequency components with distance from soma, have been studied. Four idealized neuron models and two reconstructed neurons, differing widely in their dendritic morphology, have been considered. All neuron models have passive dendritic trees and no axons. To investigate the role of the passive electrical parameters and cell morphology in determining the extracellular spike shapes, the same somatic action potentials have been used for all cell models.

Idealized neuron models

Even though a homogeneous, purely resistive extracellular medium is considered, all cells have been found to exhibit a low-pass filtering effect with distance from the neuron. This low-pass filtering effect is due to the cell's morphology, and for the larger cell models, i.e., the long, finite ball-and-stick model and reconstructed pyramidal cell model of Fig. 6 as well as the infinite ball-and-bush model and infinite ball-and-cloud model of Fig. 7, this causes a nearly linear relationship between the spike width and distance from soma in the sub- $100\text{-}\mu\text{m}$ range. This was also observed by Gold et al. (10) for compartmental models incorporating a host of active conductances. The smaller cell models of Figs. 6 and 7 also show this linearity close to soma, but the spike widths tend to increase sublinearly as the distance from soma passes $50 \mu\text{m}$ and often flattens out beyond $100 \mu\text{m}$.

The low-pass filtering effect and the decay of the extracellular peak-to-peak amplitudes are governed by a combination of the number of dendrites, their diameters and lengths, and their geometrical arrangement. A key parameter giving qualitative insights into these phenomena is the frequency-dependent AC length constant $\lambda_{AC}(f)$, defined in Eq. 10. This constant is a weighted measure of the distance from soma where current crosses the membrane in a dendritic stick with a sinusoidally varying somatic membrane potential. In an infinite-stick dendrite, $\lambda_{AC}(f)$ will generally depend on the dendritic diameter d , membrane capacitance C_m , membrane resistivity R_m , and axial resistivity R_i . However, for typical action-potential frequencies ($f \gtrsim 100$ Hz), it will effectively be independent of the membrane resistivity, i.e., $\lambda_{AC}^\infty(f) \propto \sqrt{fd/R_i C_m}$. For soma distances much shorter than the length constants $\lambda_{AC}^\infty(f)$ of the dominant frequencies in the action potential, the extracellular potential will be

dominated by the contribution from the soma currents, and the amplitude will typically scale as $d^{3/2}R_i^{-1/2}C_m^{1/2}/r$ (Eq. 22). Far away from soma the amplitude will decay faster than $1/r$, but the exact form will depend on the geometrical arrangement of the dendrites. For the dipolar infinite ball-and-stick model the amplitude will typically scale as $d^2R_i^{-1}/r^2$, but in the lateral direction the amplitude will typically scale as $d^{5/2}R_i^{-3/2}C_m^{-1/2}/r^3$. A linear quadrupolar ball-and-stick model consisting of a soma and two opposing (identical) infinitely long dendritic sticks would generally have spike amplitudes scaling as $d^{5/2}R_i^{-3/2}C_m^{-1/2}/r^3$. Our highly symmetric ball-and-star model has no dipole or quadrupole moments, and in the far-field limit the amplitude will typically scale as $d^{7/2}R_i^{-5/2}C_m^{-3/2}/r^5$. In models with finite dendrites of length l the length constant $\lambda_{AC}(f)$ will have an upper bound corresponding to half the dendritic length. Thus unless $\lambda_{AC}^\infty(f)$ is much smaller than $l/2$ for all dominant action-potential frequencies, the length constant will be affected by the finite dendrites. This will affect the parameter dependence of the spike amplitude (as exemplified for the *ball-and-star models* in Fig. 9), but not the form of the distance-decay in the far-field limit (see *ball-and-star models* in Fig. 10).

The low-pass filtering effect is directly manifested by the increase in spike width with increasing soma distance. Very close to a somatic point current, the contributions from the high-frequency components inherent in the action potential will be amplified ($|\mathbf{T}| \propto \sqrt{f}$) resulting in a narrow extracellular spike (see *inset* in Fig. 3 B). When moving away from the soma, the dendritic currents will play a larger role, and the contributions from each frequency component will be qualitatively described through the length constant $\lambda_{AC}(f)$. For distances much larger than $\lambda_{AC}(f)$, the contribution from each dendritic stick will approximately be given by a dipolar decay from a dipole with length $\lambda_{AC}(f)$. Thus high frequencies corresponding to short $\lambda_{AC}(f)$ will decay faster with distance than low frequencies with large $\lambda_{AC}(f)$. The extracellular spike will thus lose more signal power at the higher frequencies than at the lower frequencies resulting in a temporally wider spike. When the distance is much larger than $\lambda_{AC}(f)$ for all relevant action-potential frequencies, there will be no further change in the extracellular spike shape with distance.

From a technical spike-recording point of view, distances up to $\sim 100 \mu\text{m}$ are the most important; for larger distances the spike amplitudes are so low that it is difficult to extract spikes from the background noise level (4). For our ball-and-stick models we see in Fig. 6 and Fig. 10 that the amplitude decay with distance varies from $\sim 1/r$ (near soma) to $\sim 1/r^2$ in this distance range. For our stellate-shaped idealized modes (ball-and-star, ball-and-bush, ball-and-cloud) we see in Fig. 7 and Fig. 10 that the amplitude decay varies from $\sim 1/r$ to $\sim 1/r^3$. In these examples we further observed very similar amplitudes for our models with finite and infinite dendritic lengths for distances up to $100 \mu\text{m}$, even when the dendritic

sticks were as short as $200 \mu\text{m}$ as in our finite ball-and-star, ball-and-bush, and ball-and-cloud models. The spike widths were, however, seen in Fig. 7 to be strongly reduced by the finite stick lengths for distances larger than $\sim 50 \mu\text{m}$.

It has been proposed that the extracellular potential is proportional to the temporal derivative of the somatic membrane potential (see discussion in (23)). This would, in the context of our modeling, imply that the transfer function \mathbf{T} in Eq. 8 should be proportional to the frequency f . For our idealized model built up of dendritic sticks this is seen to never be the case; close to the soma, $|\mathbf{T}|$ has been found to be proportional to \sqrt{f} for the most dominant frequencies inherent in the action potential, while further away $|\mathbf{T}|$ has been found to be either independent of f or proportional to f^{-n} where n is a positive exponent.

Reconstructed neuron models

For the reconstructed pyramidal cell the amplitude is seen in Fig. 6 to decay as $1/r^n$ with an exponent n of ~ 2 for the smallest distances considered ($r \sim 20 \mu\text{m}$). The stellate cell of in Fig. 7 is seen to have a similar decay for small distances. Thus a monopole limit is not reached for these cells. Similar short-distance decays are seen for the idealized ball-and-bush and ball-and-star models in Fig. 7. The absence of an observed monopole limit for our two reconstructed cells presumably reflects the dense bushes of dendrites around the somas of these cells (see Fig. 1), which restrict the range for which the recording position is much closer to the soma currents than any prominent dendritic transmembrane currents.

For distances in the range $60\text{--}200 \mu\text{m}$, the exponent of the power-law decay is seen in Fig. 6 to be $n \sim 2.5$ for the pyramidal cell. For distances between 500 and $1000 \mu\text{m}$, however, the exponent was seen to be close to $n = 2$ (results not shown). This implies that the potential in the far-field limit is dominated by a dipolar term with a component in the horizontal direction (a dipole oriented along the apical dendrite would give a $1/r^3$ decay in the horizontal direction in the far-field limit). The faster decay between 60 and $200 \mu\text{m}$ may imply that a quadrupolar contribution from the basal dendrites dominates in this distance range, but that a dipolar contribution, which decays more slowly with distance, takes over for larger distances.

For the stellate cell the exponent of the power-law decay appears to be $n \sim 3$ in the range $60\text{--}100 \mu\text{m}$, while for distances between 100 and $200 \mu\text{m}$ n appears to be ~ 2 . Again, a suggested interpretation is that a quadrupolar contribution dominates between 60 and $100 \mu\text{m}$, while a dipolar contribution decaying more slowly with distance takes over between 100 and $200 \mu\text{m}$.

The stick-based idealized models predict the amplitude to scale as $\sim d^{3/2}$ near the soma and as $\sim d^2$ ($\sim d^{5/2}$) in the far-field limit if a dipole (quadrupole) contribution dominates the extracellular spike potential. Further, the spike amplitude

is expected to be roughly proportional to the number of sticks attached to the soma since the contributions to the extracellular potential from each stick add up linearly. In Table 1 we show the ratio between the calculated spike amplitudes for the pyramidal and stellate reconstructed cells for a set of distances to compare with predictions from these simple scaling rules. For the shortest distance considered ($r = 20 \mu\text{m}$), the ratio of the amplitudes are 3.3, in agreement with the ratios between the sums of the values of $d^{3/2}$ over all dendritic branches attached to the soma. When increasing the distance, the amplitude ratio becomes larger and reaches a maximum value of 4.0 for $r = 100 \mu\text{m}$, thus approaching the prediction from a d^2 scaling rule. For the largest distances ($r = 200 \mu\text{m}$), the ratio has dropped to 2.4, reflecting the faster decay of the pyramidal-cell amplitude ($\sim 1/r^{2.5}$) compared to the stellate-cell decay ($\sim 1/r^2$) for distances beyond $100 \mu\text{m}$ (see Figs. 6 and 7). No strong conclusions can be drawn from these results from only two reconstructed neurons, but the findings qualitatively support the suggestion from the idealized models that, for distances $< 100 \mu\text{m}$, the amplitude roughly scales as the summed value of d^m over the dendritic sticks attached to the soma where the coefficient m appears to be between 1.5 and 2.

Generalizations and implications

The scaling expressions for the transfer functions near the soma (i.e., Eq. 22) and in the far-field limit (i.e., Eqs. 23–25) were found to excellently explain the numerical results for the spike amplitudes for the idealized models. It should be noted, however, that unlike the dendrites in our idealized models, the dendrites in real neurons, including the two reconstructed cells considered here, will generally narrow with increasing distance from soma. This will affect the generated extracellular potentials. A thorough numerical study of extracellular-spike signatures for a large set of reconstructed neurons is required to make any firm statements about how these simple expressions account for the amplitude decay around real neurons. We expect that the extracellular signature around real neurons will be dominated by a combination of dipolar and quadrupolar contributions; the highly symmetric arrangement of this ball-and-star model,

which makes the octupole the first nonzero multipole contribution, is unlikely to be seen for real cells.

Both the spike widths and the spike amplitudes have been seen to be essentially independent of the membrane resistivity R_m . This result is expected to generalize as long as the membrane time constant $\tau = R_m C_m$ is much longer than the typical duration of an action potential. Thus state-dependent changes in R_m due to various levels of synaptic background activity is not expected to significantly affect the transformation from the intracellular action potential to the extracellular spike.

Our results imply that an increase in the axial resistivity R_i or the membrane capacitance C_m will tend to amplify the increase of spike-width with distance from soma (see Fig. 8). Further, an increase of the axial resistivity will generally reduce the spike amplitude, while the dependency on membrane capacitance may vary with soma distance.

The most important neuronal parameter determining the spike amplitude appears to be the number of dendrites connected to soma and their diameters. These results suggest the following rule of thumb: for distances up to $\sim 100 \mu\text{m}$ from the soma, the amplitude is roughly proportional to the sum of the cross-sectional areas of the dendrites connected to soma. This simple rule represents a compromise; close to the soma, the amplitude has in our idealized models been seen to be proportional to $\sim d^{3/2}$, while amplitudes proportional to the second or higher orders in d has been found for larger distances.

This rule should be considered when estimating cell densities on the basis of extracellular recordings (3,24,25). Neurons with few and thin dendrites would have smaller extracellular spikes than their counterparts with many thick dendrites, and therefore a smaller horizon of visibility.

In contrast to Gold et al. (10,11) all the neuron models considered here are purely passive, and, in contrast to the point-source model considered by Bédard et al. (12), a low-pass filtering effect is found even in a homogeneous, purely resistive extracellular medium. Morphologically extended neurons must show this morphology-induced low-pass filtering effect with distance. However, active ion channels or an electrically more complex extracellular medium may modify the result. Note that a frequency-dependent extracellular conductivity could directly be included in our numerical formalism

TABLE 1 Investigation of relationship between the dendritic diameters and the extracellular spike amplitude for the stellate and pyramidal neurons

Neuron	d_{av}	N	$\sum d^{3/2}$	$\sum d^2$	$\sum d^{5/2}$	A20	A60	A100	A200
Stellate	2.1	6	20	31	51	102	10.5	2.6	0.7
Pyramidal	3.0	11	66	140	332	334	39.3	10.4	1.7
Pyr./Stell.	1.4	1.8	3.3	4.5	6.5	3.3	3.7	4.0	2.4

Pyr./Stell. is the ratio between the pyramidal cell and stellate cell peak-to-peak amplitudes. d_{av} [μm] is the average dendritic diameter at the connection points between the dendrites and the soma of the neuron, N is the number of dendrites connected to soma, $\sum d^{3/2}$ [$\mu\text{m}^{3/2}$], $\sum d^2$ [μm^2] and $\sum d^{5/2}$ [$\mu\text{m}^{5/2}$] are obtained from summing the diameter at the connection points to the appropriate power over the N dendrites. The amplitudes [μV] and their ratios at the distances 20, 60, 100, and 200 μm are shown (A20, A60, A100, A200). Note that the diameters used for the dendrites at their connection-points to the soma are not the morphological diameters, but the approximated conical diameters used by the NEURON simulation tool.

for the idealized neuron models, since they explicitly sum contributions from the different frequencies contained in the intracellular action potential. A frequency-dependent extracellular conductivity $\sigma(\omega)$ (12,26) can straightforwardly be incorporated in the expressions in Eqs. 7 and 8.

The short current dipoles generating the extracellular signatures of action potentials imply that the multiunit activity (MUA) measured, e.g., with laminar multielectrodes, will be spatially more confined around the neural sources than the low-frequency potential stemming from synaptic currents onto dendrites (5–7). For such synaptic inputs the salient frequencies are expected to be so low that the typical dipole lengths will mainly be determined by the distance between the active synapses and the soma (7), i.e., much longer than the typical action-potential current dipoles. The attenuation with distance is thus expected to be weaker than for the MUA. The high-pass frequency filtering used to extract the MUA (lower cutoff at typically 750 Hz (6,7)) makes the MUA signal even more spatially confined, since only the highest AP frequencies with the shortest effective dipole lengths are retained. These results further imply that the cells having the most numerous and thickest soma-attached dendrites will give the largest contributions to the MUA.

APPENDIX A: CABLE EQUATION IN FREQUENCY DOMAIN

The cable equation for a cylinder is given by

$$\lambda^2 \frac{\partial^2 V(z, t)}{\partial z^2} = \tau \frac{\partial V(z, t)}{\partial t} + V(z, t). \quad (26)$$

For convenience the complex form of the potential is used, $V(z, t) = \hat{V}(z) \exp(j\omega t)$, and the cable equation then becomes

$$\lambda^2 \frac{\partial^2 \hat{V}(z, \omega)}{\partial z^2} = (1 + j\omega\tau) \hat{V}(z, \omega). \quad (27)$$

The general solution of this complex cable equation can be written as

$$\hat{V}(z, \omega) = \mathbf{A}e^{sz/\lambda} + \mathbf{B}e^{-sz/\lambda}, \quad (28)$$

where $\mathbf{s} = \sqrt{1 + j\omega\tau}$, $\omega = 2\pi f$ is the angular frequency, and $\tau = R_m C_m$ is the membrane time constant. From standard cable theory the axial current in a cable is

$$I_i(z, t) = -\frac{1}{r_i} \frac{\partial V(z, t)}{\partial z}, \quad (29)$$

and the transmembrane current, including both the leak and capacitive currents, is given by

$$i_m(z, t) = \frac{1}{r_i} \frac{\partial^2 V(z, t)}{\partial z^2}, \quad (30)$$

where $r_i = 4R_i/\pi d^2$; see, e.g., Johnston and Wu (17). To find the solution for a finite dendritic cable of length l with the potential $V_0(\omega)$ given as a boundary condition in $z = 0$ and a sealed-end boundary condition in $z = l$, the following boundary conditions must be imposed on Eq. 27,

$$\hat{V}(0, \omega) = V_0(\omega), \quad \hat{I}_i(l, \omega) = 0. \quad (31)$$

Here \hat{I}_i is the complex counterpart of Eq. 29. This leads to

$$\mathbf{A} + \mathbf{B} = \hat{V}_0(\omega), \quad \mathbf{A} = \mathbf{B}e^{-2sl/\lambda}, \quad (32)$$

and therefore

$$\mathbf{A} = \hat{V}_0(\omega)/(1 + e^{2sl/\lambda}), \quad \mathbf{B} = \hat{V}_0(\omega)/(1 + e^{-2sl/\lambda}). \quad (33)$$

Thus, the solution to the finite-stick cable equation in the frequency domain becomes

$$\hat{V}(z, \omega) = [e^{sz/\lambda}/(1 + e^{2sl/\lambda}) + e^{-sz/\lambda}/(1 + e^{-2sl/\lambda})] \hat{V}_0. \quad (34)$$

The total current through the somatic membrane equals the negative axial current going into the dendrite at $z = 0$. The somatic transmembrane current and linear transmembrane current density are thus found by using the complex counterparts of Eqs. 29 and 30,

$$\hat{\mathbf{I}}_s(\omega) = -\hat{\mathbf{I}}_i(0, \omega) = \frac{1}{r_i} \frac{\partial \hat{V}(z, \omega)}{\partial z} \Big|_{z=0} = \mathbf{Y}(\omega) \hat{V}_0. \quad (35)$$

Here the admittance $\mathbf{Y}(\omega)$ is given by

$$\mathbf{Y}(\omega) = \frac{\pi d^{3/2} \mathbf{s}}{2\sqrt{R_i R_m}} [1/(1 + e^{2sl/\lambda}) - 1/(1 + e^{-2sl/\lambda})], \quad (36)$$

where $\lambda = \sqrt{dR_m/4R_i}$ has been used. From Eq. 30 the complex membrane current is then found to be

$$\hat{\mathbf{I}}_m(z, \omega) = \frac{1}{r_i} \frac{\partial^2 \hat{V}(z, \omega)}{\partial z^2} = \frac{\pi s^2 d}{R_m} \hat{V}(z, \omega) = \mathbf{H}(z, \omega) \hat{V}_0, \quad (37)$$

with $\mathbf{H}(z, \omega)$ given by

$$\mathbf{H}(z, \omega) = \frac{\pi s^2 d}{R_m} [e^{sz/\lambda}/(1 + e^{2sl/\lambda}) + e^{-sz/\lambda}/(1 + e^{-2sl/\lambda})]. \quad (38)$$

APPENDIX B: EXTRACELLULAR POTENTIAL FOR BALL-AND-CLOUD NEURON

Assume N identical dendrites evenly spread out from soma in an approximately spherical pattern. This closed-field neuron is now approximated by a somatic point source and a radially symmetric dendritic cloud, created by spherically averaging the transmembrane current-source densities of the N protruding sticks. If one imagines a concentric sphere with radius r , Gauss' law for this spherically symmetric situation implies that the potential at the spherical surface only depends on the total source inside the sphere. This total source is given by the integral of the total dendritic transmembrane current inside the sphere plus the somatic current,

$$\hat{\Phi}(r, \omega) = \frac{N}{4\pi\sigma r} \left(\int_0^{r-r_s} \hat{\mathbf{I}}_m(z, \omega) dz + \hat{\mathbf{I}}_s(\omega) \right), \quad (39)$$

where r_s corresponds to the somatic radius. Because the transmembrane current $\hat{\mathbf{I}}_m$ is proportional to the double derivative of the membrane potential through Eq. 30, the fundamental theorem of calculus gives

$$\hat{\Phi}(r, \omega) = \frac{1}{r_i} \frac{N}{4\pi\sigma r} \left(\frac{d\hat{V}(z)}{dz} \Big|_{z=r-r_s} - \frac{d\hat{V}(z)}{dz} \Big|_{z=0} + r_i \hat{\mathbf{I}}_s \right). \quad (40)$$

From Eq. 35 we see that the two last terms cancel, and the potential becomes

$$\begin{aligned} \hat{\Phi}(r, \omega) &= \frac{1}{r_i} \frac{N}{4\pi\sigma r} \frac{d\hat{V}(z)}{dz} \Big|_{z=r-r_s} \\ &= -\frac{N}{4\pi\sigma r} \mathbf{I}_i(r - r_s) = \mathbf{T}(r, \omega) \hat{V}_0(\omega). \end{aligned} \quad (41)$$

For a neuron with dendritic sticks of length l , the transfer function for $r < l + r_s$ will be

$$\mathbf{T}(r, \omega) = \frac{Nd^{3/2}\mathbf{s}}{8r\sqrt{R_i R_m}} \left(\frac{e^{s(r-r_s)/\lambda}}{1 + e^{2sl/\lambda}} - \frac{e^{-s(r-r_s)/\lambda}}{1 + e^{-2sl/\lambda}} \right). \quad (42)$$

For $r \geq l + r_s$ Gauss' law imply $\mathbf{T}(r, \omega) = 0$.

APPENDIX C: AC LENGTH CONSTANT FOR INFINITE STICKS

The AC length constant is here defined as the mean value of the envelope of the sinusoidally varying (normalized) membrane current weighted with distance. For an infinite cable, this becomes

$$\lambda_{AC}^\infty(\omega) = \frac{\int_0^\infty x \sqrt{\hat{\mathbf{i}}_m \hat{\mathbf{i}}_m^*} dx}{\int_0^\infty \sqrt{\hat{\mathbf{i}}_m \hat{\mathbf{i}}_m^*} dx} = \frac{\int_0^\infty x \sqrt{e^{-qx}} dx}{\int_0^\infty \sqrt{e^{-qx}} dx} = \frac{(2/q)^2}{2/q} = \frac{2}{q}, \quad (43)$$

where the expression for the complex transmembrane current density of a stick in Eq. 5 is used. Here q is a frequency-dependent real variable defined by $q \equiv (\mathbf{s} + \mathbf{s}^*)/\lambda$, with $\mathbf{s} = \sqrt{1 + j\omega\tau}$. In normal form \mathbf{s} is given by

$$\begin{aligned} \sqrt{1 + j\omega\tau} &= (1 + (\omega\tau)^2)^{1/4} [\cos(\theta/2) + j \sin(\theta/2)] \\ &= \frac{1}{\sqrt{2}} \sqrt{1 + \sqrt{1 + (\omega\tau)^2}} + j \frac{1}{\sqrt{2}} \frac{\omega\tau}{\sqrt{1 + \sqrt{1 + (\omega\tau)^2}}}. \end{aligned} \quad (44)$$

Here De Moivre's formula for the principal value of a square root of a complex number has been used, i.e., $\theta = \arctan \omega\tau$. Trigonometric half-angle formulas and the relation $\cos(\arctan \omega\tau) = 1/\sqrt{1 + (\omega\tau)^2}$ have also been used. Therefore, q can be expressed as

$$q = 2\text{Re}[s]/\lambda = \sqrt{2} \sqrt{1 + \sqrt{1 + (\omega\tau)^2}}/\lambda, \quad (45)$$

and λ_{AC}^∞ becomes

$$\lambda_{AC}^\infty(\omega) = \lambda \sqrt{\frac{2}{1 + \sqrt{1 + (\omega\tau)^2}}}. \quad (46)$$

Alternatively, a definition of an AC length constant could be based on the complex transmembrane current density, $\hat{\mathbf{i}}_m = \frac{\pi s^2 d}{R_m} e^{-z/\lambda_{AC}^\infty} e^{j\omega t}$, which in normal form can be expressed as

$$\begin{aligned} \hat{\mathbf{i}}_m &= -\frac{\pi d}{R_m} \sqrt{1 + (\omega\tau)^2} e^{-z/\lambda_{AC}^\infty} [\sin(\omega t - kz + \phi_1) \\ &\quad - j\omega\tau \sin(\omega t - kz + \phi_2)], \end{aligned} \quad (47)$$

with

$$k = \frac{\omega\tau\lambda_{AC}^\infty}{2\lambda^2}, \quad \phi_1 = -\arctan[1/(\omega\tau)], \quad \phi_2 = \arctan(\omega\tau). \quad (48)$$

Note that for large frequencies ($\omega\tau \gg 1$) the wave number $k \approx 1/\lambda_{AC}^\infty$.

The physical transmembrane current is the real part of the complex current in Eq. 47, $i_m = \text{Re}[\hat{\mathbf{i}}_m]$. Using this as the basis for the AC space

constant, i.e., interchanging $\sqrt{\hat{\mathbf{i}}_m \hat{\mathbf{i}}_m^*}$ with $\text{Re}[\hat{\mathbf{i}}_m]$ in Eq. 43, gives a time-dependent length constant $\bar{\lambda}_{AC}^\infty(t, \omega)$. For the infinite stick we find

$$\bar{\lambda}_{AC}^\infty(t, \omega) = \frac{\lambda_{AC}^\infty}{\sqrt{1 + k^2(\lambda_{AC}^\infty)^2}} \frac{\sin(\omega t + \phi_1 - 2\arctan(k\lambda_{AC}^\infty))}{\sin(\omega t + \phi_1 - \arctan(k\lambda_{AC}^\infty))}. \quad (49)$$

For large frequencies the prefactor of Eq. 49, $\lambda_{AC}^\infty/\sqrt{1 + k^2(\lambda_{AC}^\infty)^2}$, approximates to $\lambda_{AC}^\infty/\sqrt{2}$. However, since $\bar{\lambda}_{AC}^\infty$ is time-dependent, it is not well suited for defining a typical qualitative length constant for the problem, but it should be noted that the prefactor is proportional to λ_{AC}^∞ in the high-frequency limit ($\omega\tau \gg 1$).

This work was supported by the Research Council of Norway and the Norwegian node of the International Neuroinformatics Coordinating Facility.

REFERENCES

- Nunez, P. L., and R. Srinivasan. 2006. *Electric Fields of the Brain: The Neurophysics of EEG*. Oxford University Press, Oxford, UK.
- Csicsvari, J., H. Hirase, A. Czurkó, A. Mamiya, and G. Buzsáki. 1999. Oscillatory coupling of hippocampal pyramidal cells and interneurons in the behaving Rat. *J. Neurosci.* 19:274–287.
- Viskontas, I. V., A. D. Ekstrom, C. L. Wilson, and I. Fried. 2007. Characterizing interneuron and pyramidal cells in the human medial temporal lobe in vivo using extracellular recordings. *Hippocampus.* 17:49–57.
- Buzsáki, G. 2004. Large-scale recording of neuronal ensembles. *Nat. Neurosci.* 7:446–451.
- Schroeder, C. E., A. D. Mehta, and S. J. Givre. 1988. A spatiotemporal profile of visual system activation revealed by current source density analysis in the awake macaque. *J. Neurophysiol.* 8:575–592.
- Ulbert, I., E. Halgren, G. Heit, and G. Karmos. 2001. Multiple microelectrode-recording system for human intracortical applications. *J. Neurosci. Methods.* 106:69–79.
- Einenvoll, G. T., K. H. Pettersen, A. Devor, I. Ulbert, E. Halgren, and A. M. Dale. 2007. Laminar population analysis: estimating firing rates and evoked synaptic activity from multielectrode recordings in rat barrel cortex. *J. Neurophysiol.* 97:2174–2190.
- Rall, W., and G. M. Shepherd. 1968. Theoretical reconstruction of field potentials and dendrodendritic synaptic interactions in olfactory bulb. *J. Neurophysiol.* 31:884–915.
- Holt, G. R., and C. Koch. 1999. Electrical interactions via the extracellular potential near cell bodies. *J. Comput. Neurosci.* 6:169–184.
- Gold, C., D. A. Henze, C. Koch, and G. Buzsáki. 2006. On the origin of the extracellular action potential waveform: A modeling study. *J. Neurophysiol.* 95:3113–3128.
- Gold, C., D. A. Henze, and C. Koch. 2007. Using extracellular action potential recording to constrain compartmental models. *J. Comput. Neurosci.* 23:39–58.
- Bédard, C., H. Kröger, and A. Destexhe. 2004. Modeling extracellular field potentials and the frequency-filtering properties of extracellular space. *Biophys. J.* 86:1829–1842.
- Carnevale, N., and M. Hines. 2006. *The NEURON Book*. Cambridge University Press, Cambridge, UK.
- Holt, G. 1998. A critical reexamination of some assumptions and implications of cable theory in neurobiology. Ph.D. thesis, California Institute of Technology, Pasadena, CA.
- Dayan, P., and L. F. Abbott. 2001. *Theoretical Neuroscience: Computational and Mathematical Modeling of Neural Systems*. The MIT Press, Cambridge, MA.
- Marks, R. 1960. *The Dymaxion World of Buckminster Fuller*. Reinhold, New York.
- Johnston, D., and S. M. Wu. 2001. *Foundations of Cellular Neurophysiology*, 5th Ed. The MIT Press, Cambridge, MA.

18. Zador, A., H. Agmon-Snir, and I. Segev. 1995. The morphoelectronic transform: a graphical approach to dendritic function. *J. Neurosci.* 15: 1669–1682.
19. Connor, J. A., and C. F. Stevens. 1971. Prediction of repetitive firing behavior from voltage clamp data on an isolated neurone soma. *J. Physiol.* 213:31–53.
20. Connor, J. A., D. Walter, and R. McKown. 1977. Neural repetitive firing: modifications of the Hodgkin-Huxley axon suggested by experimental results from crustacean axons. *Biophys. J.* 18:81–102.
21. Mainen, Z. F., and T. J. Sejnowski. 1996. Influence of dendritic structure on firing pattern in model neocortical neurons. *Nature.* 382: 363–366.
22. Hämäläinen, M., R. Hari, R. Ilmoniemi, J. Knuutila, and O. Lounasmaa. 1993. Magnetoencephalography theory, instrumentation, and applications to noninvasive studies of the working human brain. *Rev. Mod. Phys.* 65:413–497.
23. Henze, D. A., Z. Borhegyi, J. Csicsvari, A. Mamiya, K. D. Harris, and G. Buzsáki. 1996. Intracellular features predicted by extracellular recordings in the hippocampus in vivo. *J. Neurophysiol.* 84: 390–400.
24. Barthó, P., H. Hirase, L. Monconduit, M. Zugaro, K. D. Harris, and G. Buzsáki. 2004. Characterization of neocortical principal cells and interneurons by network interactions and extracellular features. *J. Neurophysiol.* 92:600–608.
25. Freund, T. F., and G. Buzsáki. 1996. Interneurons of the hippocampus. *Hippocampus.* 6:347–470.
26. Bedard, C., H. Kröger, and A. Destexhe. 2006. Model of low-pass filtering of local field potentials. *Phys. Rev. E.* 73:051911.